

The Large Synoptic Survey Telescope as a Near-Earth Object Discovery Machine

R. Lynne Jones¹, Colin T. Slater¹, Joachim Moeyens¹, Lori Allen², Mario Juric¹, Željko Ivezić¹, Tim Axelrod³, Jonathan Myers⁴

Abstract

We investigate the capabilities of LSST to discover Near-Earth Objects (NEOs), fast-moving objects which are challenging to track and link, and discuss the expected yield of NEO discoveries resulting from variations on the survey strategy. The typical LSST cadence uses pairs of observations over a series of nights to discover NEOs; we test this data processing strategy by empirically determining an expected false positive detection rate using DECam data and prototype LSST software. We validated that this expected rate is tractable with the Moving Object Processing Software (MOPS). Using a high-fidelity simulated survey pointing history, we evaluate the performance of the LSST baseline survey strategy for Potentially Hazardous Asteroids (PHAs) and find an expected completeness of 68% for PHAs with $H < 22$ from LSST alone. We also generate variations on the baseline survey strategy to evaluate potential methods to increase the PHA completeness. For example, extending the LSST survey by two additional years and including previously known objects increases the completeness for PHAs to 85%. Additional substantial investments in LSST software development and compute resources could provide a further boost of a few percent.

Subject headings: Near-Earth objects — Image processing – Asteroids

¹Department of Astronomy, University of Washington, Box 351580, Seattle, WA 98195, USA

²National Optical Astronomy Observatory, 950 North Cherry Avenue, Tucson, AZ 85719, USA

³University of Arizona, Steward Observatory, 933 North Cherry Avenue, Tucson, AZ 85721, USA

⁴Johns Hopkins University, Applied Physics Laboratory, 11100 Johns Hopkins Rd, Laurel, MD 20723, USA

1. Introduction

The small-body populations in the Solar System, such as asteroids, trans-Neptunian objects (TNOs) and comets, are remnants of its early assembly. Collisions in the main asteroid belt between Mars and Jupiter still occur, and occasionally eject objects on orbits that may place them on a collision course with Earth. About 20% of this near-Earth Object (NEO) population pass sufficiently close to Earth orbit such that orbital perturbations with time scales of a century can lead to intersections and the possibility of collision. These objects that pass within 0.05 AU of Earth’s orbit are termed potentially hazardous asteroids (PHAs). In order to improve quantitative understanding of this hazard, in December 2005 the U.S. Congress directed¹ NASA to implement a NEO survey that would catalog 90% of NEOs with diameters larger than 140 meters by 2020 (known as the George E. Brown, Jr. mandate). It is estimated that there are about 6,000 such objects (Harris & D’Abramo 2015). For a compendium of additional information about NEOs and PHAs and an up-to-date summary of discovery progress, see NASA’s NEO webpage².

The completeness level set by the Congressional mandate could be accomplished with a 10-meter-class ground-based optical telescope, equipped with a multi-gigapixel camera and a sophisticated and robust data processing system (see NASA-commissioned reports by Stokes et al. 2003; National Research Council 2010). The Large Synoptic Survey Telescope³ (LSST), currently being constructed, is such a system. A concise LSST system description, discussion of science drivers, and other information, are available in Ivezić et al. (2008). The LSST baseline strategy for discovering Solar System objects is predicated on two observations of the same field per night, spaced by a few tens of minutes, and a revisit of the same field with another pair of observations within a few days. The main reason for two observations per night is to help association of observations of the same object from different nights, as follows. The typical distance between two nearby asteroids on the Ecliptic, at the faint fluxes probed by LSST, is a few arcminutes (counts are dominated by main-belt asteroids). Typical asteroid motion during several days is larger (of the order a degree or more) and thus, without additional information, detections of individual objects are “scrambled”. However, with two detections per night, the motion vector can be estimated. The motion vector makes the linking problem much easier because positions from one night can be approximately extrapolated to future (or past) nights. The predicted position’s uncertainty is typically

¹National Aeronautics and Space Administration Authorization Act of 2005 (Public Law 109-155), January 4, 2005, Section 321, George E. Brown, Jr. Near-Earth Object Survey Act

²<http://neo.jpl.nasa.gov/neo/>

³www.lsst.org

of the order of several arcminutes, rather than a degree, which effectively “de-scrambles” detections from different nights (for a detailed discussion of this algorithm, see Appendix B).

Early simulations of LSST performance presented by Ivezić et al. (2007) showed that the 10-year baseline cadence would result in 75% completeness for PHAs greater than 140 m (more precisely, for PHAs with $H < 22$; see §5.6 for further discussion). They also suggested that with additional optimization of the observing cadence, LSST could achieve 90% completeness. An example of such an optimization was discussed by Ivezić et al. (2008) who reported that, to reach 90% completeness, about 15% of observing time would have to be dedicated to NEOs, and the survey would have to run for 12 years. The latest LSST simulation results, presented here, yielded a completeness of $\sim 68\%$ for PHAs with $H < 22$, using the current 10-year baseline survey. The minor differences in reported completeness compared to older LSST studies are attributable to differences in simulated NEO populations and other modeling details (such as improved hardware understanding).

These completeness estimates are based on an implicit assumption that 3 pairs of observations obtained within a 15-30 day wide window are sufficient to recognize that these observations belong to the same object, and to estimate its orbital parameters (the same criterion has been used in NASA studies⁴). This so-called linking of individual detections into plausible orbital tracks will be performed using a special-purpose code referred to as the Moving Object Processing System (MOPS). MOPS and its algorithms are significantly more advanced than anything previously fielded for this purpose (Denneau et al. 2013).

The described LSST strategy for discovering moving objects has been questioned (e.g., Grav et al. 2016) on two grounds:

- A large number of false detections due to problems with image differencing software may make linking problem prohibitively hard for MOPS. In particular, this objection is motivated by the experience from extant surveys, such as Pan-STARRS and the Catalina Sky Survey.
- Modifications of LSST baseline cadence, including image depth, sky coverage and cadence, required to reach 90% completeness level, have not yet been explicitly demonstrated using detailed operations simulations, and made available to the community.

We aim to address these critiques here: the two major questions addressed by our study can be informally stated as “Will MOPS work?” and “If MOPS works, what fraction of NEOs will LSST discover?”.

⁴See <http://neo.jpl.nasa.gov/neo/report2007.html>

We use a combination of sophisticated simulations and real datasets to address these questions. The main analysis components presented here include:

1. Analysis of the performance of prototype LSST image differencing software, with emphasis on the rate and properties of false detections (so-called “false positives”), using DECam imaging data.
2. Analysis of the linking of asteroid detections in the presence of a large number of false positives, using MOPS and simulated observations.
3. Analysis of a large number of modified observing cadence simulations, coupled with NEO population models, to forecast discovery rates.

We demonstrate that i) MOPS can cope with the anticipated false detection rates in LSST difference images, and that ii) the NEO discovery performance of the LSST baseline cadence can be appreciably boosted by adequate modifications of the observing strategy. In §2 we provide a brief overview of LSST and its strategy for discovering moving Solar System objects. We discuss the performance of prototype LSST image differencing pipeline in §3, and MOPS performance in §4. Modifications of the baseline cadence designed to boost NEO/PHA completeness are described in §5, and our results are summarized and discussed in §6.

2. LSST Strategy for Discovering Solar System Objects

We briefly describe the LSST system design and observing strategy, and discuss in more detail image processing and moving object detection.

2.1. A Brief Overview of LSST Design

LSST will be a large, wide-field ground-based optical telescope system designed to obtain multiple images covering the sky that is visible from Cerro Pachón in Northern Chile. The current baseline design, with an 8.4m (6.7m effective) primary mirror, a 9.6 deg^2 field of view, and a 3.2 Gigapixel camera, will allow about 10,000 square degrees of sky to be covered every night, with typical 5σ depth for point sources of $r \sim 24.5$ mag (AB). The system is designed to yield high image quality (with a median delivered seeing in the r band of about 0.8 arcsec) as well as superb astrometric and photometric accuracy⁵. The total survey area will include $\sim 30,000 \text{ deg}^2$ with $\delta < +34.5^\circ$, and will be imaged multiple times in six bands, $ugrizy$, covering the wavelength range 320–1050 nm. The project is scheduled to begin the regular survey operations at the start of next decade.

LSST will be operated in a fully automated survey mode. About 90% of the observing time will be devoted to a deep-wide-fast survey mode which will uniformly observe a 18,000 deg^2 region about 800 times (summed over all six bands) during the anticipated 10 years of operations, and yield a coadded map to a depth of $r \sim 27.5$. These data will result in catalogs including about 40 billion stars and galaxies, that will serve the majority of the primary science programs. The remaining 10% of the observing time will be allocated to special projects such as a Very Deep and Fast time domain survey⁶.

2.2. LSST Observing Strategy

As designed and funded (by the U.S National Science Foundation and the Department of Energy), LSST is primarily a science-driven mission. The LSST is designed to achieve goals set by four main science themes:

1. Probing Dark Energy and Dark Matter;

⁵For detailed specifications, please see the LSST Science Requirements Document, <http://ls.st/srd>

⁶Informally known as “Deep Drilling Fields”.

2. Taking an Inventory of the Solar System;
3. Exploring the Transient Optical Sky;
4. Mapping the Milky Way.

Each of these four themes itself encompasses a variety of analyses, with varying sensitivity to instrumental and system parameters. These themes fully exercise the technical capabilities of the system, such as photometric and astrometric accuracy and image quality.

The current baseline survey strategy is designed to maximize the overall science returns, including Solar System science, rather than just the completeness of NEO/PHAs brighter than $H = 22$ (though the two goals are highly interrelated). Discovering and linking objects in the Solar System moving with a wide range of apparent velocities (from several degrees per day for NEOs to a few arc seconds per day for the most distant TNOs) places strong constraints on the cadence of observations. The baseline strategy requires closely spaced pairs of observations, two or preferably three times per lunation. The visit exposure time is set to 30 seconds to minimize the effects of trailing for the majority of moving objects. The images are well sampled to enable accurate astrometry, with anticipated absolute accuracy of at least 0.1 arcsec (and possibly an order of magnitude better when calibrated with upcoming Gaia’s dataset, Gaia Collaboration et al. 2016).

LSST observations can be simulated using the LSST Operations Simulator tool (OpSim, Delgado et al. 2014). OpSim runs a survey simulation with given science-driven desiderata, a software model of the telescope and its control system, and models of weather and other environmental variables. The output of such a simulation is an “observation history”, which is a record of times, pointings, used filter, and associated environmental data and telescope activities throughout the simulated survey. This history can be examined using the LSST Metrics Analysis Framework tool (MAF, Jones et al. 2014) to assess the efficacy of the simulated survey for any particular science goal or interest⁷. These tools – OpSim and MAF, and the sky brightness, throughput and sensitivity modeling – are part of the LSST simulation effort (Connolly et al. 2014), which provides high-fidelity tools to evaluate LSST performance.

⁷For examples of such analysis, see <http://ls.st/xpr>

2.2.1. LSST Baseline Survey Simulation

As the system understanding improves, the baseline survey strategy and the telescope model are updated, generally on a yearly schedule. The current reference baseline simulated survey is known as *minion_1016*. It includes 2.4 million visits collected over 10 years, with 85% of the observing time spent on the main survey and the rest on various specialized programs. The median number of visits *per night* is 816, with 3,026 observing nights. The median airmass is 1.23 (the minimum attainable altitude for the LSST telescope is 20 deg.). In the *r* band, the median seeing (FWHM) is 0.81 arcsec, and the median 5σ depth for point sources is 24.16 (using the best current estimate of the fiducial 5σ depth at airmass of one, $m_5(r)=24.39$).

There are a few known problems with this simulation, including twilight sky brightness estimates that are too bright, the moon avoidance that is not as aggressive as it could be, and observations that are biased towards west, away from the meridian. The implied impact of these shortcomings on NEO completeness estimates is a few percent (the performance of this simulated cadence in NEO context is discussed in detail in §5). An improved simulation, that will presumably rectify these problems, will become available by the end of 2017.

2.3. Overview of LSST Data Management and Image Processing

The images acquired by the LSST Camera will be processed by LSST Data Management software (Jurić et al. 2015) to a) detect and characterize imaged astrophysical sources and b) detect and characterize temporal changes in the LSST-observed universe. The results of that processing will be reduced images, catalogs of detected objects and their measured properties, and prompt alerts to “events” – changes in astrophysical scenery discovered by differencing incoming images against older, deeper, images of the sky in the same direction (*templates*). More details about the main algorithms and pipeline design are available in Appendix A.

LSST will use two methods to detect moving objects in difference images:

1. Detecting trailedd motion on the sky: objects trailedd by more than 2 PSF widths (corresponding to motion faster than about 1 deg/day) will be easily detectable as trailedd. Two trailedd detections within 20–60 minutes in a single night will be sufficient to identify an object as an NEO candidate,
2. Inter-night linking of pairs of detections from the same night: this technique will recover objects moving too slow to be measurably elongated in a single exposure.

We note that sources detected in difference images (DIASources in LSST parlance, see Appendix A) will also include false detections, colloquially known as *false positives*. In addition to false positives due to instrumental artifacts and software glitches, in this context they will also include detections of true astrophysical transients (e.g. gamma-ray burst afterglow) that will not be associated with static sources (e.g. stars and galaxies). Estimates of expected false positive rates are discussed in §3.

2.4. The Basic Strategy for Linking Detections into Orbits

The LSST strategy for linking detections into orbits assumes the following main steps:

1. Detections in difference images (obtained during the same night), that do not have a nearby static object (e.g. variable stars) within a small exclusion radius (a fraction of an arcsecond, but possibly larger for brighter stars), are linked into tracklets. There will be of the order a million tracklets per observing night (see §B.1).
2. At least three tracklets obtained in a 15-30 day wide window are linked into candidate tracks, using kd-trees and pre-filtering steps based on tracklets' positions and motion vectors (see §B.2). These pre-filtering steps result in about the same number of false tracks as true tracks on the Ecliptic (of the order a million), with the completeness depending on population (e.g. main-belts asteroids vs. NEOs) and chosen tunable pre-filtering parameters (generally well above 90%).
3. Candidate tracks are then filtered further (pruned from false tracks) using the initial orbit determination (IOD) and measurement uncertainties for the positions of all six detections. Given typical astrometric errors (0.15 arcsec for the faintest objects, see §B.2.2) and a fiducial tracklet density of 450 deg^{-2} , the probability of a chance alignment of a *single* false detection within 5σ astrometric tolerance from a fiducial 10 degree long trajectory is only about 10^{-4} . For a trajectory constrained by 3 detections, the probability that 3 more detections will line up by chance is thus about 10^{-12} (compared to $\sim 10^7$ detections per night). Hence, the number of false tracks which could pass IOD-based filtering is negligible, as well as the incompleteness induced by this step. Indeed, the only reason for track pre-filtering in the second step is to decrease the number of candidate tracks that are processed by the more computationally expensive IOD.

False positives, be it false detections, false tracklets or false tracks, are assumed not be an issue because IOD will efficiently and reliably filter out false tracks due to high-accuracy

astrometry and well-understood simple Keplerian model predictions. Therefore, the essential question is whether the resulting number of false tracks, and the corresponding IOD step, can be handled with available computing resources. As discussed in detail in §4 and in Appendix B, even with computing resources quite modest compared to the sizing of LSST data processing system, the handling of the three steps above is not an issue.

3. Analysis of Image Differencing Performance

LSST will detect motion and flux variability by differencing each incoming image against a deep template (built by combining multiple images of the same region). Sources in difference images, called **DIASources**, will be detected at a signal-to-noise ratio (SNR) threshold of $\nu = 5$ (for more details, please see Appendix A). Up to about $1,000 \text{ deg}^{-2}$ astrophysical, real, detections (e.g. variable stars) are expected in LSST image differencing, including up to about 500 deg^{-2} asteroids on the Ecliptic. In addition to real detections, there are false detections due to both imaging or processing artifacts, and an irreducible background of false detections caused simply by statistical noise fluctuations in the background. In a typical LSST difference image, the expected density of false positives due to background fluctuations is about 60 deg^{-2} (see below for details)—much lower than the expected rate of astrophysical detections.

However, historically surveys have reported detection rates in image differencing that are much higher, depending on the survey; see Denneau et al. (2013); Kessler et al. (2015); Goldstein et al. (2015). For example, Pan-STARRS1 (PS1) reported a transient detection rate as high as $8,200 \text{ deg}^{-2}$ (Denneau et al. 2013). For a “menagerie” of PS1 artifacts (with memorable names such as *chocolate chip cookies, frisbee, piano, arrowhead, UFO*), see Fig. 17 in Denneau et al. (2013). They reported that “Many of the false detections are easily explained as internal reflections, ghosts, or other well-understood image artifacts, ...”. As discussed in §B.1, such a high false positive rate is at the limit of what could be handled even with the substantial computing power planned for LSST.

Fortunately, Pan-STARRS1 was only a first-generation experiment and, over the past decade, subsequent surveys have learned tremendously from the PS1 experience. There are surveys running today, such as Dark Energy Survey, which have largely solved the key problems that PS1 has encountered. Major improvements to hardware include CCDs with significantly fewer artifacts (e.g. DECam, see below; LSST) and optical systems designed to minimize ghosting and internal reflections (e.g. LSST). Improvements to the software include advanced image differencing pipelines (e.g., PTFIDE for the Palomar Transient Factory and the Zwicky Transient Facility) and various machine learning classifiers for filtering false positives. For example, Goldstein et al. (2015) used a Random Forest classifier with the Dark Energy Survey data and cleaned their sample of transient detections from a raw false:true detection rate ratio of 13:1 to a filtered rate of 1:3. This significant improvement is mainly due to morphologically much simpler false positives; for example, compare Fig. 1 in Goldstein et al. (2015) to Fig. 17 in Denneau et al. (2013).

Here we summarize an analysis of image differencing performance based on DECam data and difference images produced and processed using prototype LSST software (Slater

et al. 2016). This analysis demonstrates that the false positive rate anticipated for LSST is significantly below the threshold for successful deployment of MOPS, as will be discussed in Section 4.

3.1. LSST Image Differencing Pipeline and Data Processing

The LSST prototype image differencing and analysis code largely derives from the HOT-PANTS package (Becker 2015), and was used for surveys such as SuperMACHO (Becker et al. 2005) and ESSENCE (Miknaitis et al. 2007). While this software is functional as-is, it is expected that the ultimate LSST pipeline will include improved methods for handling observations at high airmass and the effects of differential chromatic refraction due to the Earth’s atmosphere. Nevertheless, in this work we conservatively assume that the pipeline used for LSST will have the same performance as the current code.

Before presenting the results of this analysis, we summarize the expected behavior of false positives due to background fluctuations.

3.2. False Detections due to Background Fluctuations

Due to background fluctuations around the mean, it is possible to get false detections even at a high SNR threshold. The number of such detections, as a function of the threshold SNR, the number of pixels and seeing, can be computed using the statistics of Gaussian random fields. For an image with a Gaussian background noise, convolved with a Gaussian point spread function (PSF) with width σ_g (in pixels), the number of peaks, N , above a given SNR threshold, ν , is given by

$$N(> \nu) = \frac{n_{row} * n_{col}}{2^{5/2} \pi^{3/2} \sigma_g^2} \nu e^{-\nu^2/2} \quad (1)$$

where n_{row} and n_{col} are the number of pixel rows and columns in the image. This expression was verified empirically by LSST data management team using image simulations⁸. For 4k by 4k LSST sensors the pixel size is 0.2 arcsec, and for a nominal seeing of 0.85 arcsec and $\nu = 5$, $N(> \nu) = 59 \text{ deg}^{-2}$.

It is generally not well appreciated just how steep is the dependence of $N(> \nu)$ on ν due to the exponential term. Changing the threshold from 5 to 5.5 decreases the expected

⁸See <https://github.com/lsst/W13report>

rate by a factor of 12, and the rate increases by a factor of 9.7 when the threshold is changed from 5 to 4.5. In practice, an empirical estimate of the background noise is used when computing the SNR for each detected source. When this estimate is incorrect, e.g. due to reasons discussed below, then the implied detection threshold is wrong, too. For example, if the noise is underestimated by only 10%, the computed SNR will be too large by 10%, and the adopted threshold $\nu = 5$ will actually correspond to $\nu = 4.5$ – and thus the sample will include 9.7 times as many false positives due to background fluctuations! Hence, the noise in difference images has to be estimated to high accuracy.

3.2.1. *The Impact and Treatment of Correlated Noise*

When the LSST pipeline convolves the science image to match the PSF of the template image, the per-pixel variance in the image is reduced, and at the same time correlations between neighboring pixels are introduced. This violates the assumption made by standard image processing algorithms that each pixel is an independent draw from a Poisson distribution. The per-pixel noise reduction is reflected in the variance plane that accompanies each exposure during processing, but the covariance between pixels is not tracked. The significance of detections and the uncertainties on source measurements is then estimated based on this incomplete information provided by the variance plane, leading to a biased detection threshold.

The magnitude of this effect can be large—using only the per-pixel variance measurements can result in underestimating the true noise on PSF-size scales by 20% or more. A detection threshold of $\nu = 5$ thus actually corresponds to $\nu = 4$, and it is easy to see using eq. 1 that this error results in an increase in the number of false positives by a factor of $\sim 70!$

A histogram of the number of sources detected in difference images, as a function of SNR computed using forced photometry measurements, is shown in the right panel of Figure 1. The blue line shows the expected counts given by eq. 1, in good agreement with data. When the SNR is estimated incorrectly due to correlated noise (left panel), the distribution clearly ramps up at a much higher SNR value and results in numerous false positives that are mis-classified as $> 5\sigma$ detections.

Tracking the covariance caused by multiple convolutions is a planned feature for the LSST software stack, but is not currently implemented. Previous surveys, such as Pan-STARRS1, have used a small covariance “pseudo-matrix”, which tracks the covariance between a small region of neighboring pixels, and then assumed that this relationship between pixels is constant across an image (Paul Price, priv. comm.). This method avoids the cre-

ation of the full N_{pixels} by N_{pixels} covariance matrix, which is impractically large and mostly empty.

In the interim, for this analysis we have mitigated the problem by utilizing forced photometry of **DIASources** on individual images (that is, before convolution to match their PSFs). This produces both flux measurements and associated uncertainties which are not affected by covariance, enabling us to accurately set a SNR threshold that recognizes and rejects all **DIASources** with $\nu < 5$. This mitigation step will be unnecessary once the image covariance tracking is properly implemented in the LSST stack. Alternative solutions such as image “decorrelation” (Reiss & Lupton 2016), or the Zackay et al. (2016) image differencing algorithm, would also alleviate the covariance problem, and tests of these methods in the LSST pipeline are ongoing.

3.3. Testing the LSST Pipeline with DECam

The Dark Energy Survey (DES) is an optical/near-infrared survey that aims to probe the dynamics of the expansion of the universe and the growth of large scale structure by imaging 5,000 sq. deg. of the southern sky. DECam, the imaging camera developed for DES, is sufficiently similar to LSST camera to enable an informative study of false positive rates: DECam includes 62 mosaicked deep-depletion CCDs, with a total pixel count of 520 Mpix over its 3 deg² field of view, and has a similar filter complement as LSST (Flaugher et al. 2015).

The data we use here are a subset of a DECam NEO survey (PI: L. Allen, NOAO) conducted in the first half of 2013. The data for a given field consist of 40-second exposures separated by about five minutes. Due to the difference in telescope aperture, these images are about 1 mag shallower than the 30 second visits by LSST. We used data for five different fields, each with between three and five visits for a total of 15 “science” visits plus 5 template visits. While this section will present statistics based on this subset of the survey’s data, during the course of this work a much larger set of 540 visits from the same survey was also processed and produced false positive rates broadly consistent with this initial data (on average the 540 visits have fewer false positives by about 30% than the small subset.)

From the NOAO archive we obtained images that had already had instrumental signature removal applied by the DECam Community Pipeline. Each image was processed through the initial LSST pipeline for background subtraction, PSF determination, source detection and measurement (collectively termed “processCcd” in the LSST pipeline). For each field, we arbitrarily selected one of the visits to serve as the “template” exposure, against

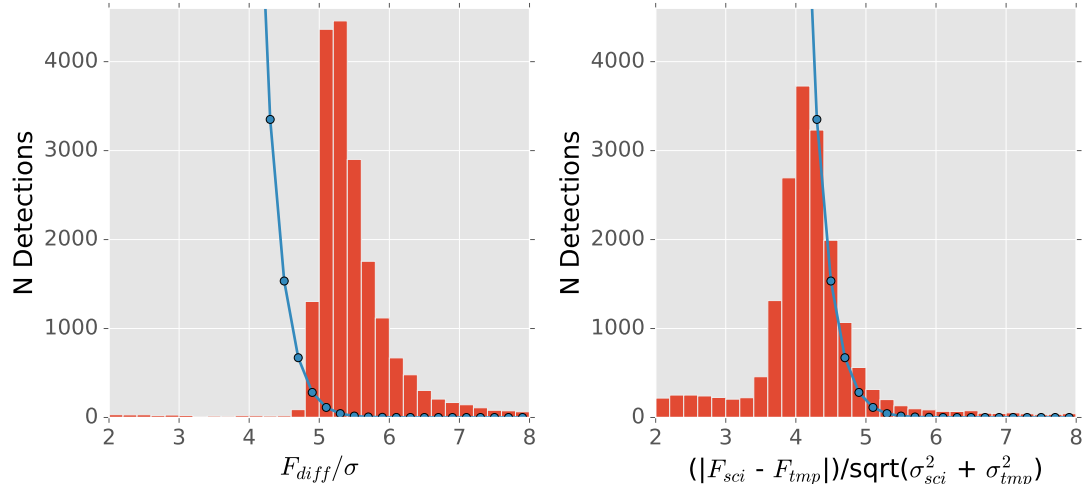


Fig. 1.— Histogram of the reported SNR of sources measured in the difference images, using two different SNR estimates: SNR estimated from forced photometry on the input images (right), and SNR (incorrectly) estimated using the variance plane of the difference images (left). The blue lines indicate the expected SNR distribution based on Gaussian background noise. The difference between these two histograms illustrates the strong impact of the SNR mis-estimation. Using the correct SNR values, the vast majority of putative $> 5\sigma$ detections become $< 5\sigma$ detections and can be disregarded.

which the other visits in the field are differenced. Sources are then detected in the difference image to produce **DIASources**, and forced photometry performed in both the original “science” and “template” exposures at the position of any **DIASource**.

In LSST operations, coadded prior exposures will be used as templates for image differencing rather than single visits, which will reduce the noise in template images. In this study, our use of single visits instead of coadded templates implies that some moving objects or transients will appear as negative sources in the difference images. We simply disregard these sources since our goal is to mimic LSST operations rather than discover all possible transients in this dataset.

3.3.1. *The Transient and False Positive Rates in DECam Images*

Using the $> 5\sigma$ cut based on SNR estimated using forced photometry, the average number of positive **DIASources** is $\sim 1000 \text{ deg}^{-2}$, with some fields having as few as 500 deg^{-2} . A large fraction of these detections are the result of stars that have been poorly-subtracted and left significant residuals in the difference image. It is a common problem for subtracted stars to exhibit “ringing” with both positive and negative excursions, and these images are no exception. Because the focus of this work is on detecting moving objects rather than variable stars or transients, we have not attempted to correct these subtraction artifacts. Instead, we simply exclude difference image detections where there is significant ($> 15\sigma$) flux in both the science and template images at the position of the **DIASource**—that is, we exclude all **DIASources** that overlap with a static source (of course, some may be truly variable sources). The area lost due to this masking is less than 1% of the total sky. Again, this is not the intended behavior of LSST during production, but instead a temporary expedient we can use for conservatively estimating the system’s performance. One could view this step as a “poor man’s” machine learning step.

After excluding all **DIASources** associated with stationary objects, the remaining candidate moving object detections number on average $\sim 350 \text{ deg}^{-2}$. This sample includes asteroids, false positives, and possibly some true astrophysical transients that are not associated with stationary objects (gamma-ray burst afterglows, very faint variable stars with sharp light curve maxima, etc.). To improve the estimate of the fraction of these remaining objects that are false, we visually classified one focal plane of detections either as obvious imaging artifacts, obvious PSF-like detections, or unidentifiable detections. Approximately 25% of the reported detections were clearly some sort of uncorrected artifact (we did not pursue the cause of individual artifacts), 25% appeared to be acceptable PSF-like features, and the remaining 50% were ambiguous or had too low of signal to noise to be able to classify.

Therefore, a conservative upper limit on the fraction of false positives is 75%, corresponding to a rate of 263 deg^{-2} . Given the size of DECam pixels (0.263 arcsec) and typical seeing of about 1.1 arcsec ($\sigma_g = 1.8 \text{ pix}$), the expected rate due to background fluctuations is 33 deg^{-2} , leaving a rate of 230 deg^{-2} as “unexplained” false positives.

The SNR distribution of this sample is proportional to $1/\text{SNR}^{2.5}$, which is similar to distributions expected for astrophysical objects. This fact implies that the sample might be dominated by true astrophysical transients; nevertheless, we adopt the above conservative upper limit of 75%.

3.3.2. Scaling DECam Results to LSST Performance

The LSST false positive rate due to background fluctuations is about twice as large as for DECam because of smaller pixels and better seeing. The scaling with pixel size and seeing for “unexplained” false positives is not obvious because their cause is unknown. For example, if they are a pixel-induced effect, their rate should be scaled up by the square of the ratio of angular pixel sizes, or a factor of 1.72. If they are instead dominated by true astrophysical transients, they should not be scaled at all. We adopt the most conservative option and scale up the DECam rate for “unexplained” false positives to 396 deg^{-2} . In addition, there will be 60 deg^{-2} false positives due to background fluctuations (Equation 1, referenced to the median seeing of 0.85 arcsec).

The total false positive rate of $\sim 450 \text{ deg}^{-2}$ anticipated for LSST is thus comparable to the rate of astrophysical transients. Again, this estimate of the false positive rate is very conservative and it would not be very surprising if it turns out to be several times smaller.

3.3.3. Spatially Correlated Transients

We also investigated whether **DIASources** from different difference images are correlated in focal plane coordinates. A large number of such correlated detections could result in a substantial increase of tracklets and tracks. We analyzed 4 visits with 60 CCDs each, and found 24 **DIASources** that match to within two pixels. We did not find any correlation at larger radii. These 24 **DIASources** show tendencies for certain CCDs but the counts are too low to make a robust conclusion. Visual inspection shows that many are near parts of an image where a defect (such as a cosmic ray, bad column, bleed trail, etc) had been interpolated over, though for some the cause is unclear. The implied density of correlated **DIASources** is about 2.3 deg^{-2} , rendering this effect relatively unimportant.

4. Analysis of Moving Object Processing System Performance

The linking of individual detections from difference images into plausible orbital tracks will be performed using a special-purpose code referred to as the Moving Object Processing System (MOPS). There are several slightly modified versions of MOPS in use by various projects; the original version was developed collaboratively by Pan-STARRS and LSST, and is described in Denneau et al. (2013). MOPS employs a two-step processing: first pairs of detections from a given night are connected into *tracklets*, and then at least three tracklets are associated into a candidate *track*. Realistic MOPS simulations show high linking efficiency (>99%; Denneau et al. 2013) across all classes of Solar System objects. The core algorithmic components of MOPS are *findTracklets* and *linkTracklets* kd-tree algorithms by Kubica et al. (2007). *findTracklets* links **DIASources** from a single night to produce *tracklets*, and *linkTracklets* links tracklets from at least three nights to produce candidate *tracks* (assuming quadratic motion in each coordinate; the LSST version also accounts for topocentric corrections). Candidate tracks produced by MOPS are then filtered using initial orbital determination (IOD) step, which is executed using a stand-alone code (e.g. OrbFit, Milani et al. 2008; OpenOrb, Granvik et al. 2009).

Given empirically estimated false positive rates expected for LSST, discussed in the preceeding section, in this section we show that MOPS performance is already adequate - MOPS requires significantly less computing capacity than planned for other LSST data processing needs. In addition to reporting the results of numerical experiments with MOPS, we also analyze them using analytic and semi-analytic results for the rates of false tracklets and false tracks.

4.1. A Summary of LSST tests of MOPS

As a part of the Final Design Review preparations, the LSST team has developed an enhanced prototype implementation of MOPS and analyzed its behavior. Here we summarize the main results of that work; a detailed report is publicly available (Myers et al. 2013).

Simulated **DIASources** were based on a Solar System model by Grav et al. (2011). The model includes about 11 million objects; about 9 million are main-belt asteroids. Observations span 30 days and were selected from a simulated baseline cadence (at that time, the baseline simulation was OpSim3.61, which in this context is statistically the same as the current baseline cadence, *minion_1016*). The number of tracklets and tracks, the runtime, and the memory usage were studied as functions of the false positive detection rate. The rate was varied from none to four times the asteroid detection rate (100 deg^{-2}). The highest

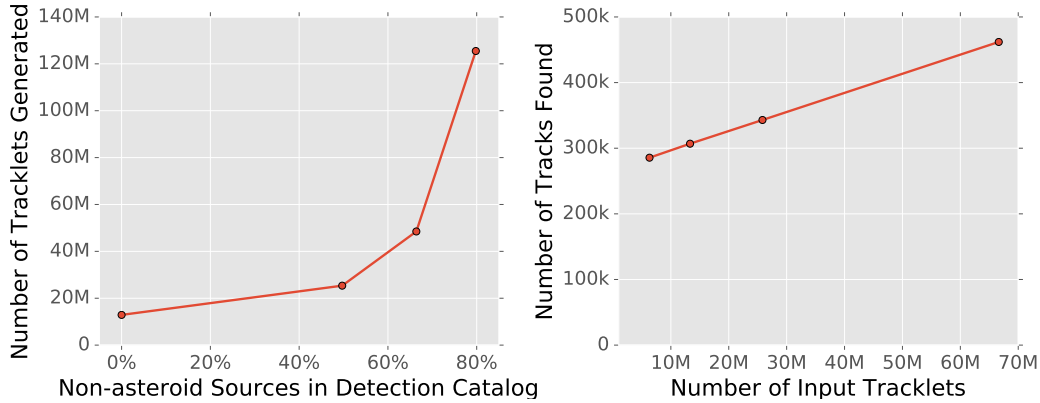


Fig. 2.— A summary of MOPS tests for the dependence of the number of tracklets (left) and tracks (right) on the false positive detection rate. As the rate of false positive detections increases from none to four times the asteroid detection rate, the number of tracklets increases by about an order of magnitude. At the same time, the number of candidate tracks increases by only about 50%.

rate corresponds to the expected false positive detection rate for LSST ($\rho_{FP} = 400 \text{ deg}^{-2}$).

Tests were run with 16 threads on single 16 CPU node on Gordon cluster at San Diego Supercomputing Center (in 2011). Due to computational constraints, a $v < 0.5 \text{ deg/day}$ velocity limit for pairing detections into tracklets was imposed. For similar reasons, the filters that were imposed on track fitting were not optimized, artificially reducing the yield. As we now understand the algorithmic scalings much better (see Appendix B), it is clear that these unoptimized filters have no major impact on the simulation results and derived conclusions.

As expected, the addition of false positive detections increases the number of tracklets and tracks, the runtime, and the memory usage. For the 4:1 false:true detection rate ratio, compared to case with no false positive detections, the number of tracklets increases by about a factor of 10, the number of tracks by about 50%, and runtime increases by about a factor of 3. For the 4:1 false:true detection rate ratio, the runtime with 16 CPUs is 33 hours, with maximum memory usage of about 80 GB.

4.2. Understanding MOPS Performance

The rather slow increase of the number of tracks with false positive detection rate (only 50% increase although the number of tracklets increased by a factor of 10) is somewhat unexpected. We have developed analytic and semi-analytic analysis to better understand

the scaling of the number of tracklets and tracks with false positive detection rate and other relevant parameters. Details of this analysis are provided in Appendix B. Here we briefly discuss the main results.

The increase of the number of tracklets with false positive detection rate, ρ_{FP} , shown in left panel in Figure 2, is well described by eq. B5. In particular, the number of tracklets approximately increases proportionally to $(C_1 + C_2 \rho_{FP}^2)$, where C_1 and C_2 do not depend on ρ_{FP} . As both the full analytic result and the simulations show, false tracklets quickly outnumber true tracklets even at low false detection rates, resulting in the observed ρ_{FP}^2 behavior.

While the number of tracklets is dominated by the false positive detections, in baseline LSST cadence and nominal noise assumptions under which the MOPS simulations were run ($\rho_{FP} \leq 500 \text{ deg}^{-2}$), the number of tracks is not dominated by spurious detections—instead it is dominated by true tracks and mislinkages between true objects. This is due to the fundamental feature of MOPS: the 4-dimensional space of tracks (two coordinates and two velocity vector components) is sparse at up to moderate levels of contamination, and at the tested noise levels false tracklets are effectively filtered out. This behavior accounts for the slow growth in tracks in the right panel of Figure 2.

As we evaluate the impact of different survey parameters, we can assess the number of tracks that would be generated (and thus require IOD processing) using the analytic results developed in Appendix B. For a given window width and false detection density, the number of false tracks per search window that would arise from false detections is given by

$$N^{falsetracks} = 4.5 \times 10^6 \left(\frac{N_w}{30 \text{ day}} \right)^8 \left(\frac{\rho_{FP}}{400 \text{ deg}^{-2}} \right)^{3.7}. \quad (2)$$

This expression is valid around fiducial values and assumes $\rho_{ast} = 100 \text{ deg}^{-2}$. The number of true tracks is of the order 10^6 ; therefore, with the baseline window $N_W = 15$ the contribution of false detections is small, while in the enhanced NEO cadences with $N_W = 30$ the contribution is only a factor of a few times the number of true tracks.

4.3. Required Computing Resources for MOPS and IOD Processing

Given the modest computing resources used in MOPS tests described above, the runtime and memory usage results bode well for LSST processing. Assuming a 1000-core machine dedicated to LSST moving object processing (corresponding to about 1% of the anticipated total LSST compute power at the National Center for Supercomputing Applications), MOPS

runtime for producing candidate tracks should not exceed an hour, assuming sufficient parallelization can be achieved.

The IOD step can also be handled with anticipated resources and is trivially parallelizable. The number of available IOD computations for a compute system with N_{core} cores and allocated runtime $T_{runtime}$ can be estimated as

$$N_{IOD} = 3.6 \times 10^8 \left(\frac{0.1 \text{ sec}}{T_{IOD}} \right) \left(\frac{T_{runtime}}{10 \text{ hr}} \right) \left(\frac{N_{core}}{1000} \right). \quad (3)$$

where T_{IOD} is the time it takes to perform one IOD computation on a single core. Estimates of T_{IOD} are of the order 50 mas (S. Chesley, priv. comm.), considerably below the fiducial value of 100 mas adopted here. Given that the expected number of candidate tracks to filter using IOD is well below 10^7 , it should be possible to accomplish the IOD step in well under an hour. Alternatively, it is plausible that a 100-core machine might be sufficient for LSST moving object processing (assuming no engineering safety margin).

5. LSST Observing Cadence Optimization to Enhance PHA Completeness

By observing in pairs of visits – a strategy validated in the previous sections – rather than triplets or quads of visits in each night, we can increase sky coverage and improve the survey efficiency. However, even within this constraint, there are multiple approaches to surveying the sky. In this section we evaluate the effects of varying the LSST observing strategy and the resulting PHA completeness.

This evaluation is carried out using a combination of the LSST Operations Simulator (OpSim) and the LSST Metrics Analysis Framework (MAF). The LSST Metrics Analysis Framework (MAF) is a user-oriented, python package for evaluating the pointing history from these simulated surveys in light of particular science goals or interests. The various metrics coded in the MAF framework can be calculated for any given simulated survey and compared as simulation parameters are changed in OpSim. This permits a thorough investigation of the trades between different observing strategies, in terms of the effect on multiple science goals, including the PHA completeness. We first describe the basic steps in our simulations, then describe the baseline and modified LSST simulated surveys, and then discuss our results.

5.1. Simulations of LSST Asteroid Discoveries

The basic components of our end-to-end simulation of asteroid discovery, described in detail below, include

1. *NEO Population Modeling.* Orbital parameters are used to generate asteroid positions during the simulated survey duration for a simulated or properly debiased extant NEO population. The population needs to adequately sample color, size and other properties. A database of such positions evaluated with an adequate time step is available as an input to MAF.
2. *Survey Cadence Modeling.* A series of LSST pointings with instrumental metadata and observing conditions is generated by OpSim. In addition to boresight positions, the camera orientation and selected filter, available metadata enable the computation of instrumental sensitivity (limiting magnitudes).
3. *Asteroid Optical Flux Modeling.* Optical flux from an arbitrary asteroid needs to be computed as a function of the positions of the Sun, the asteroid and Earth, and asteroid physical properties (e.g., size and color). This model is implemented in MAF.

4. *Source Detection Modeling.* Given the instrument model, observing conditions and asteroid flux, the signal-to-noise ratio is estimated and used to compute detection probability. This model is implemented in MAF.
5. *Detection Linking Modeling.* Instead of running MOPS, a model that emulates MOPS performance is used to significantly speed up the computations. This model is implemented in MAF.
6. *Completeness Estimation.* Given a list of “discovered objects”, and the input population, the completeness is estimated as a function of asteroid properties (e.g. size) and various other parameters (e.g. observing strategy). This model is implemented in MAF.

We proceed to describe these models in more detail, and then discuss the baseline and several modified LSST surveys, and the corresponding PHA completeness estimates.

5.1.1. NEO Population Modeling

We use random samples from the synthetic solar system model (S3M) presented in Grav et al. (2011) in order to model completeness for NEOs and PHAs. We have chosen a sample of 2000 NEOs from the Grav et al. (2011) NEO population, which is based on the Bottke et al. (2002) model. We chose a separate sample of 2000 PHAs from the same model, by choosing NEOs with a MOID ≤ 0.05 AU. The PHA population is useful for evaluating PHA completeness directly; the NEO population is useful for comparison to other survey evaluations. A plot of the a, e, i distributions for these PHAs and NEOs is shown in Figure 3.

With this small set of orbits, we then assume that the H magnitude distribution is independent of the orbital distribution. For most small body populations, including the PHA population larger than 140 m in diameter, this is approximately true. Assuming an independent distribution, each orbit can be “cloned” from the fiducial H magnitude to a range of values covering the interesting sizes for analysis; this allows the analysis to use a large number of objects at each H value, without requiring extensive resources to generate ephemerides for a much larger set of orbits. We use the small population of 2000 NEOs or PHAs and clone them to a range of H magnitudes between $H=11$ and $H=28$ using $dN/dH = 10^{\alpha H}$, with $\alpha = 0.3$ (Schunová-Lilly et al. 2017). We have verified with a larger simulated set of NEOs that reducing the population from 10,000 to 2000 objects does not change the calculated survey completeness significantly.

Using the details of the input population, MAF generates the expected observations of

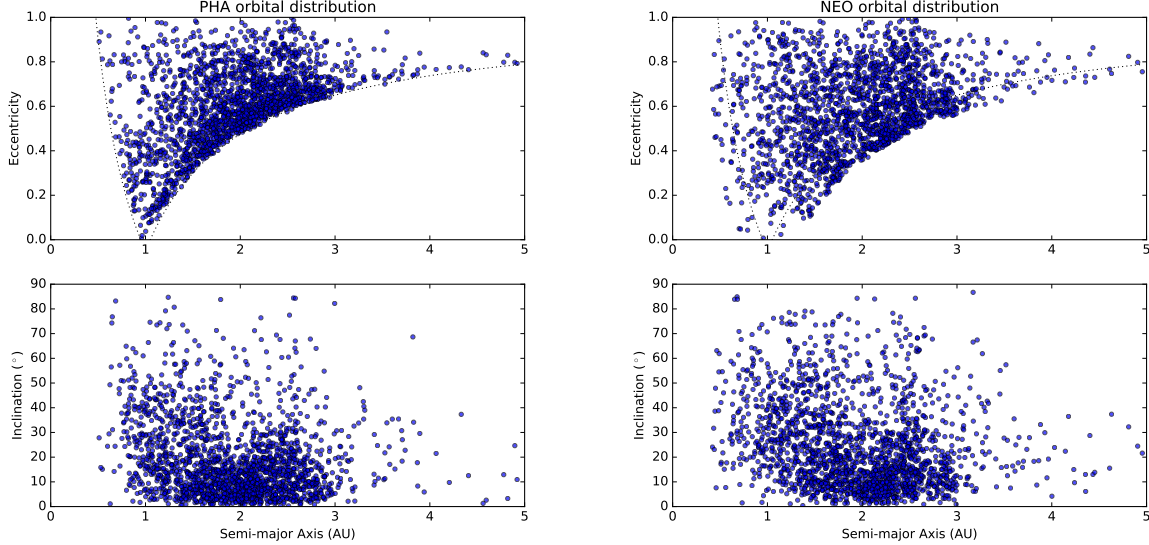


Fig. 3.— The eccentricity and inclination distributions, as a function of semi-major axis, of the PHAs (left) and NEOs (right) used in this analysis. Both populations were randomly sampled from the S3M model (Grav et al. 2011), a synthetic solar system model based on the Bottke et al. (2002) NEO orbital distribution. NEOs are defined as objects with $q < 1.3$ AU; PHAs are defined as having a Minimum Orbit Intersection Distance (MOID) with Earth of less than 0.05 AU (implying $q \leq 1.05$ AU) and having $H \leq 22$.

each object using the pointing history from a specific OpSim simulated survey. Ephemerides are generated using OpenOrb (Granvik et al. 2009) for a closely spaced grid of times (typically every 2 hours), and then interpolated to the exact times of each OpSim pointing.

5.1.2. Survey Cadence Modeling

The LSST Operations Simulation (OpSim, Delgado et al. 2014) is a python software package that generates a realistic pointing history, with the time, filter, location, astronomical conditions, weather conditions, and predicted point-source 5σ limiting magnitude, for each LSST visit for, typically, ten years. This pointing history is generated using weather data (cloudiness and seeing) from the Cerro Pachón site and a high-fidelity model of the telescope itself (including slew and settle time and dome movement, for example), combined with a parameterized set of observing proposals that determine how the scheduling algorithm attempts to gather observations. By configuring OpSim with different parameters for the observing proposals, we can generate a series of simulated surveys which prioritize different

science goals. The LSST baseline survey and its modifications designed to enhance the PHA completeness are described in detail in §5.2 below.

5.1.3. Asteroid Optical Flux Modeling

Given H magnitude for an object, its apparent magnitude in Johnson’s V band can be easily computed given the positions of the object, the Sun and the observer (e.g. Jurić et al. 2002). Magnitudes, or fluxes, in any other optical and near-IR band (in case of LSST, u , g , r , i , z , and y) can be computed from V magnitude by specifying a spectrum for each object. We have assumed that our entire NEO population has the same spectral energy distribution as C-type main-belt asteroids. The computed color transformations for LSST bandpasses are listed in Table 1. Choosing the spectral energy distribution of S-type main-belt asteroids instead results in <1% changes in completeness. These simulation-based colors were verified using SDSS observations (Ivezić et al. 2001) and analogous computations with SDSS bandpasses.

5.1.4. Source Detection Modeling

If the object is within the LSST field of view, its predicted position, velocity, and apparent V magnitude (calculated from the fiducial H magnitude associated with the orbit) is recorded along with information about the simulated observation itself (such as the seeing, limiting magnitude, filter, and boresight RA/Dec). The full LSST camera footprint (see Figure 4), including chip gaps, is used to determine whether an object is within the field of view.

MAF also calculates signal-to-noise (SNR) loss due to trailing for each observation,

Table 1. Color transformations from Johnson’s V band to LSST bandpasses, for C and S type asteroids.

Type	$V - u$	$V - g$	$V - r$	$V - i$	$V - z$	$V - y$
C	-1.53	-0.28	0.18	0.29	0.30	0.30
S	-1.82	-0.37	0.26	0.46	0.40	0.41

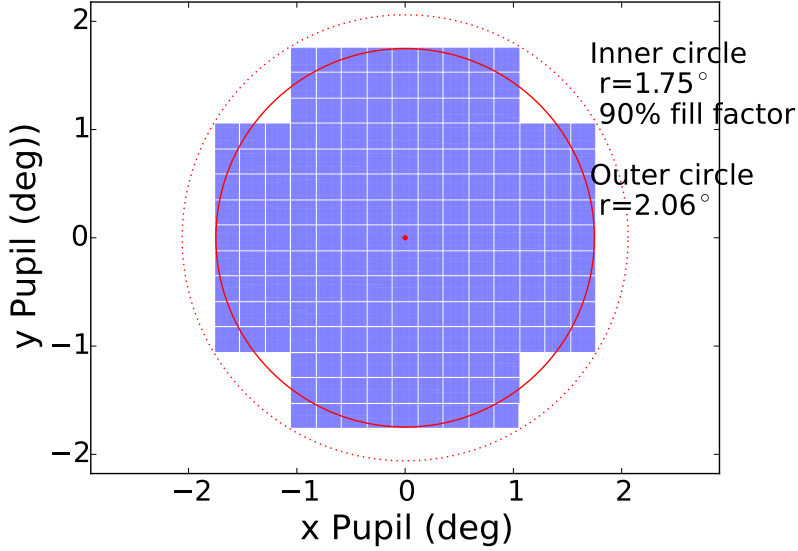


Fig. 4.— Model of the LSST camera footprint, including chipgaps and CCD + raft layout.

which is required when evaluating whether a particular object is detectable in a given observation. Trailing losses occur whenever the movement of an object spreads its photons over a wider area than a simple stellar point spread function (PSF). There are two aspects of trailing loss to consider: SNR losses and detection algorithm losses. The first is the irreversible degradation in SNR that occurs because the trailed object includes a larger number of background pixels in its footprint, compared to a stationary PSF. The second effect, detection loss, occurs because source detection software is optimized for detecting point sources; a stellar PSF-like matched filter is used when identifying sources that pass above the defined threshold. This filter is non-optimal for trailed objects but losses can be mitigated with improved software (*e.g.* detecting to a lower PSF-based SNR threshold and then using a variety of trailed PSF filters to detect sources). When considering whether a source would be detected at a given SNR using typical source detection software, the sum of SNR trailing and detection losses should be used. With an improved algorithm optimized for trailed sources (implying additional scope for LSST data management), the smaller SNR losses should be used instead.

Our simulations of these effects show that both types of trailing losses can be fit well

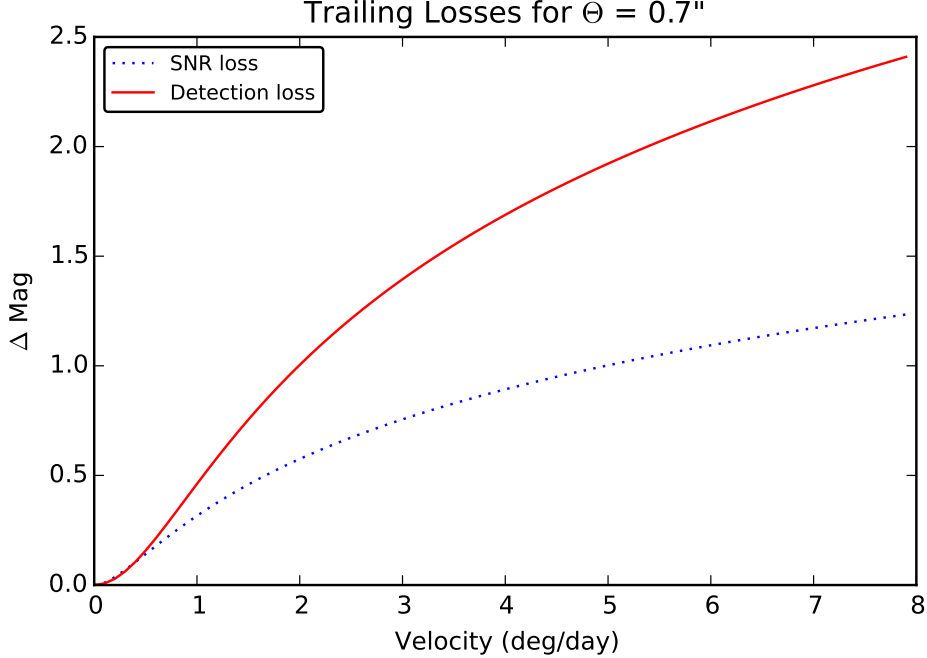


Fig. 5.— Trailing losses for 30 second LSST visits, assuming seeing of $0.7''$. The dotted line shows SNR trailing losses, the solid line indicates cumulative losses that also account for non-optimal detection algorithm. With software improvements the latter detection losses can be mitigated. At the fiducial $v = 1$ deg/day, the SNR loss is ~ 0.3 mag, and non-optimal detection algorithm contributes an additional loss of ~ 0.16 mag.

with the same functional form:

$$\Delta m = -1.25 \log_{10} \left(1 + \frac{ax^2}{1+bx} \right) \quad (4)$$

$$x = \frac{v T_{exp}}{24\theta} \quad (5)$$

where v is the velocity (in deg/day), T_{exp} is the exposure time (in seconds), and θ is the FWHM (in arcseconds). For trailing SNR losses, we find $a = 0.67$ and $b = 1.16$; for the cumulative loss, that includes both SNR and detection losses, we find $a = 0.42$ and $b = 0$. An illustration of the magnitude of these trailing loss effects for 0.7 arcsec seeing is given in Figure 5.

We calculate the probability of detecting a particular source given its magnitude m and the 5σ limiting magnitude m_5 (after accounting for trailing losses) using a logistic function

$$P = \left[1 + \exp \left(\frac{m - m_5}{\sigma} \right) \right]^{-1}. \quad (6)$$

where $\sigma=0.12$ describes the width of the completeness falloff (Annis et al. 2014). A source is randomly classified as detected using the probability P . We also evaluate more optimistic discovery criteria using only SNR trailing losses (i.e. without taking detection losses into account), as well as detections to SNR=4 instead of SNR=5.

5.1.5. *Detection Linking Modeling*

Once we have computed the set of all visits in which a given object was within the field of view and detected, we locate subsets of these visits that match our target discovery criteria. These criteria generally consist of a given number of visits within a specified time span within a single night, followed by a given number of additional nights (each with the same required number of visits in the same time span) falling within a specified time window. The basic criteria is a pair of visits in each night occurring within 60 minutes, repeated for 3 nights within a 15 day time window. However, we also evaluate the effect of varying the discovery criteria to require triplets or quads of visits within a single night, and increase the length of the search window from 15 to 30 days.

5.1.6. *Completeness Estimation*

With each unique set of discovery criteria, we have a record of what objects would be “discovered” at each H value. With this we calculate the differential discovery completeness, the fraction of objects discovered at a given H magnitude. To turn this into a cumulative discovery completeness, we simply integrate over H , assuming a given H distribution for the population (recall that we use $dN/dH = 10^{\alpha H}$, with $\alpha = 0.3$).

5.2. OpSim Simulated Surveys

5.2.1. *The LSST Baseline Survey*

The current baseline observing strategy for LSST is represented by our reference run, `minion_1016`. This simulated survey contains observations balanced between several different observing proposals:

1. The Wide, Fast, Deep (WFD) proposal (also known as the Universal proposal) is the primary LSST survey, expected to receive about 90% of the observing time and to

cover 18,000 deg² of sky. In the baseline observing strategy, this proposal is configured to obtain visits in pairs spaced about 30 minutes apart, and will typically return to each field about every 3-4 days, balancing the six *ugrizy* filters. The footprint for the WFD proposal covers approximately +5° to –60° in declination, with a full range of RA values except for a region around the Galactic plane. This declination range corresponds to an airmass limit of about 1.3 when the fields are at an Hour Angle of ±2 hours. In `minion_1016`, the WFD proposal receives 85% (2,083,758) of the total number of visits.

2. The North Ecliptic Spur (NES) proposal is an extension to the WFD to reach the northern limits of the Ecliptic plane (+10 degrees), and allows higher airmass observations. The visit timing is similar to the WFD, although the *u* and *y* filter are not requested in this region. In the baseline observing strategy, `minion_1016`, each NES field requests about 40% of the total number of WFD visits per field when considering *griz* filters only (304 visits per field in *griz* vs 795 visits per field in *griz* in WFD), and receives 6% (158,912) of the total number of visits.
3. The Deep Drilling Fields (DD) proposal includes a set of single pointings that are requested in extended sequences; currently these sequences are *grizy* visits, with additional coverage in *u* band. Each sequence requires about an hour of observing time, and is repeated every few days. In `minion_1016`, there are 5 DD fields, 4 of which correspond to fields which have been officially selected by the Project and announced to the community; these five fields receive 5% of the total visits.
4. The Galactic Plane (GP) proposal covers the region with high stellar density around the Galactic plane not covered by the WFD. This proposal requests a small number of visits in each of the six *ugrizy* filters, with no timing constraints. In `minion_1016`, this proposal receives 2% of the total visits.
5. The South Celestial Pole (SCP) proposal is an extension of the WFD footprint to cover the region south of –60° declination. Like the GP, this proposal requests a small number of visits in each of the six *ugrizy* filters, with no timing constraints. In `minion_1016`, this proposal receives 2% of the total visits.

The footprint of these various proposals in the baseline `minion_1016` reference run is shown in Figure 6. In each proposal, the individual visits are 30 seconds long, consisting of two back-to-back coadded 15 second exposures.

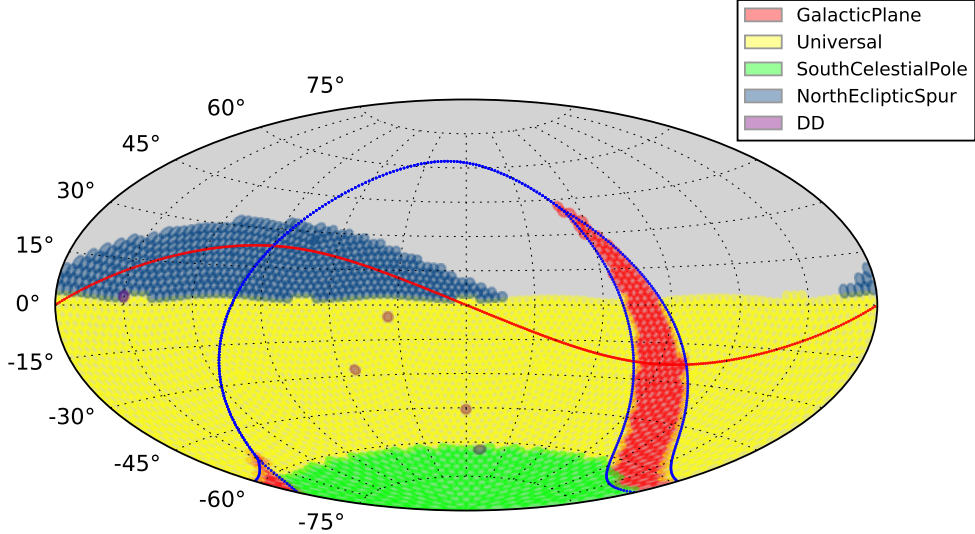


Fig. 6.— The footprints of the various proposals included in the baseline observing strategy, represented by reference run `minion_1016`.

5.2.2. Modified Surveys

A series of additional OpSim simulated surveys were created with parameters intended to improve the efficiency of discovering PHAs and increase the cumulative PHA completeness. They span the range from minor modifications to extreme changes that would jeopardize other LSST science goals. We consider the latter in order to assess what would be ultimate performance of an LSST-like system fully dedicated to NEO surveying.

Extra ecliptic spur visits: The first cadence change is simply to increase the number of visits requested for the NES proposal in *griz*, to increase the likelihood of discovering objects near the northern portion of the Ecliptic plane, and to extend the survey from 10 years to 15 years, increasing the discovery rate of PHAs with long synodic periods. Other proposals remain the same as in `minion_1016`. Reprioritizing the NES relative to the WFD results in the WFD receiving 69% (2,561,334 visits over 15 years) of the total visits and the NES receiving 24%, compared to 85% and 6% respectively in the baseline strategy. The resulting simulated survey is `astro_lsst_01_1016`. We consider `astro_lsst_01_1016` as our 'baseline PHA' run, as it makes minimal changes to the overall survey strategy while attempting to be more PHA friendly.

Longer ecliptic visits: This simulation introduce an Ecliptic Band (EB) proposal, requesting observations with visit timing similar to the WFD in the *griz* filters, but with

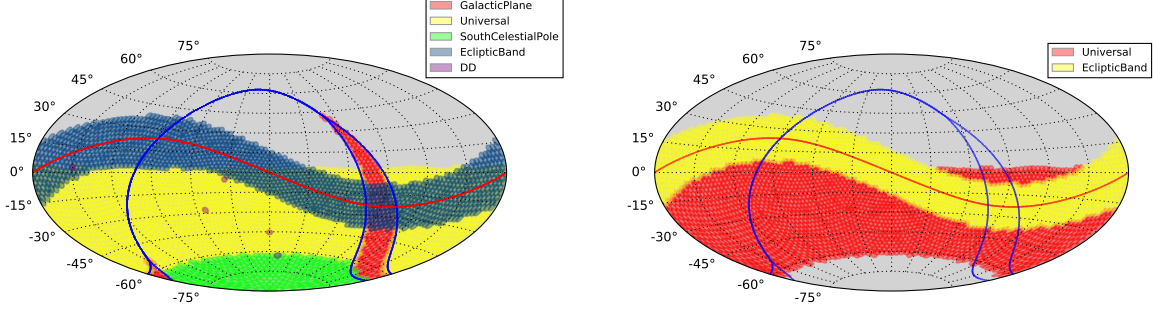


Fig. 7.— The footprints of the proposals, including the Ecliptic Band proposal, used in the NEO-optimized simulated surveys `astro_lsst_01_1015` (the “longer ecliptic visits” survey, left) and `astro_lsst_01_1017` (the “NEO-focused” survey, right). The `astro_lsst_01_1017` survey only includes two proposals.

field locations surrounding the Ecliptic Plane $\pm 15^\circ$ and extending down to the WFD where the Ecliptic reaches its northernmost range. This proposal replaces the NES proposal, and requests longer 60 second visits in order to reach deeper limiting magnitudes. Other proposals remain the same as in `astro_lsst_01_1016`. With this reprioritization, the WFD receives 44% (1,159,319) of the total visits while the EB receives 53%; the simulated survey is `astro_lsst_01_1015`.

NEO-focused survey: An attempt at an aggressively NEO-optimized survey was also created, where modified versions of the EB and WFD proposals are used. The visit timing in each proposal is the same as the standard WFD visit timing (a pair of visits separated by about 30 minutes), however the WFD footprint is changed to simply cover the entire area between 0° and -60° declination except for the EB footprint. The EB and WFD proposals request observations in only *gri* filters, with 30 second visits in the WFD and 60 second visits in the EB. No other proposals are included. The resulting simulated survey is `astro_lsst_01_1017`.

5.3. Completeness analysis results

In the baseline reference run, `minion_1016`, with the baseline discovery criteria (pairs of visits occurring within 60 minutes and repeated for 3 nights within a 15 day time window), we find a cumulative completeness at $H \leq 22$ of 65.6% for our PHA input population (see Figure 8). This should be considered our initial baseline PHA completeness, as it uses the reference run and the baseline MOPS and data management requirements.

From this baseline, we can evaluate the effects of changing both the survey design (reallocating telescope resources) and the discovery criteria, which effectively sets the computational resources. There is an interplay between discovery criteria and survey design – as an obvious example, discovery criteria requiring triplets of visits per night instead of pairs will result in much different completeness results if the survey was designed to only request two visits per night rather than three. Likewise, some changes in survey design work best with changes to the discovery criteria; for example, lengthening the visit time increases the detection losses and pushing source detection to the “trailing loss” limit is required for a significant improvement in completeness. While we compare discovery criteria within a single simulated survey as much as possible, there are some changes in discovery criteria which must be compared between different surveys using different observing strategies.

All the completeness results presented below assume that no objects are known prior to LSST survey, and thus are biased low. For example, by assuming that 43% PHAs would be discovered by the start of LSST survey, Grav et al. (2016) showed that the final PHA completeness for LSST baseline survey would be boosted by 11%. We discuss our own independent estimates of this effect in §5.4.

5.3.1. *Modified Discovery Criteria & Computational Strategies*

Using only the baseline `minion_1016` and not changing the survey strategy, we can explore the impact on PHA completeness of changing the discovery criteria. These correspond primarily to the different columns of Table 2, and include:

- extending the MOPS window for linking pairs of detections from the nominal 15 day window to a 30 day window: this increases completeness by about 3%, although with an estimated increase in the compute requirements by about an order of magnitude (see Appendix B).
- using sources detected down to $\text{SNR}=4$ instead of $\text{SNR}=5$: this increases completeness by about 3%, although with an estimated increase in the compute requirements by about two orders of magnitude (see §3.2).
- enhancing source detection algorithms to mitigate detection losses to the trailing loss level: with the 30 second visits in the baseline `minion_1016`, this only increases completeness by a very small amount, about 0.5%.

Increasing the MOPS linking window from 15 to 30 days achieves a substantial gain in completeness for the baseline survey (or any survey with a maximum visit time of 30

Table 2. The cumulative completeness for PHAs with $H \leq 22$ for various survey strategies (rows) and discovery criteria (columns). In addition to changing the overall duration of the survey (12 years instead of 10), the completeness is shown for different track linking windows ($N_w = 15$ or 30 days), enhanced detection algorithms to reduce trailing losses (“Trail Det”), and pushing the individual detection threshold from SNR= 5 to SNR= 4. These are primarily computational changes, while the various rows show different survey cadences. These range from the current baseline, to adding additional visits or longer visits in the ecliptic region, to focusing the majority of the time on performing a NEO-focused survey.

Simulation	10 year survey			12 year survey			
	$N_w=15$	$N_w=30$	$N_w=30$	$N_w=15$	$N_w=30$	$N_w=30$	$N_w=30$
				Trail Det	SNR=4		
LSST baseline	65.6	68.4	69.1	—	—	—	—
Extra ecliptic visits	66.1	69.8	70.5	70.5	73.9	74.8	77.1
Longer ecliptic visits	63.2	67.5	70.5	67.3	71.7	74.5	75.7
NEO-focused cadence	66.5	70.3	72.3	70.2	73.8	75.8	77.2

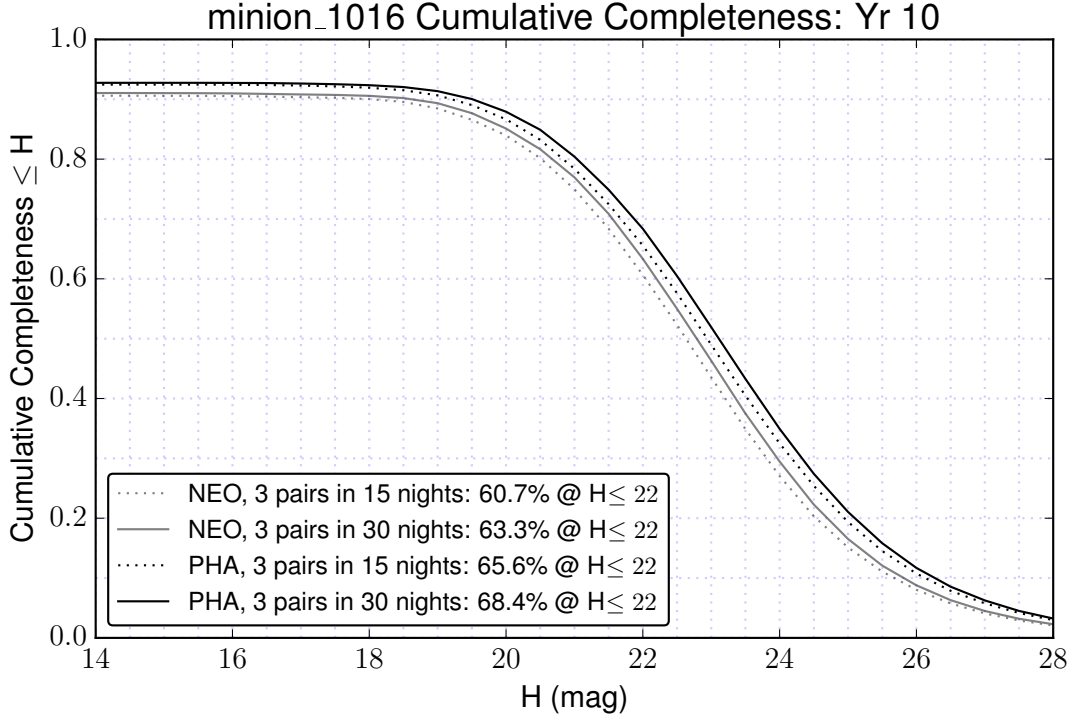


Fig. 8.— The cumulative completeness for PHAs and NEOs, as a function of absolute magnitude H , for the baseline cadence minion_1016. The completeness is below 100% at the bright end (large size limit) because some objects have synodic periods longer than the survey duration (and thus effectively “hide” behind the Sun), and some are visible but do not receive the required number of observations due to telescope scheduling.

seconds) without a significant computational cost. The increased window allows more opportunities to capture the PHAs in a set of observations which meet the discovery criteria. It is worthwhile to note that the current OpSim behavior does not prioritize capturing large chunks of contiguous sky, and often leaves gaps in coverage from night to night. This behavior is likely related to the increase in completeness going from 15 day windows to 30 day windows; with the large LSST field of view, after 30 days the areal coverage will be much more evenly distributed than after 15 days. Changes to the scheduling algorithm to favor covering contiguous blocks of sky⁹ are likely to improve the completeness even further. Completeness could potentially be increased by over 10% by better scheduling; this is illus-

⁹A similar modification of the baseline cadence, the so-called “rolling cadence”, is also favored by the supernovae science programs. A release of a series of simulated surveys implementing this idea is anticipated for late 2017.

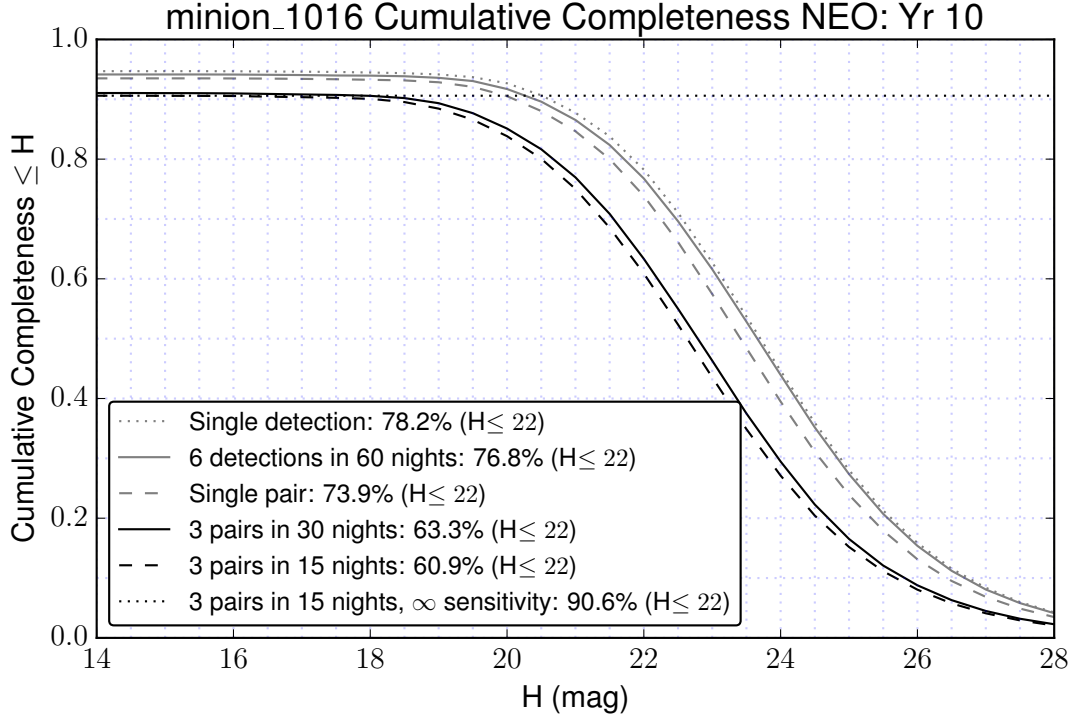


Fig. 9.— The cumulative completeness for NEOs, as a function of absolute magnitude H , for the baseline cadence minion_1016, considering a variety of detection requirements. The completeness is below 100% at the bright end (large size limit) because some objects have synodic periods longer than the survey duration (and thus effectively “hide” behind the Sun), and also because some objects do not receive the required number of observations within the ‘window’. It is not due to the limited sensitivity of the LSST system, as can be seen by the “3 pairs in 15 nights, ∞ sensitivity” line, which shows the completeness expected when the discovery requirement is 3 nights with pairs of observations within a 15 night window but assuming an infinitely sensitive survey. The potential gains with better optimized scheduling (observing larger contiguous chunks of sky, for example), can be seen in the difference between the single pair of detections or 6 separate detections within 60 nights, vs. 3 pairs of detections in 15 or 30 nights (indicating potential gains of over 10% in completeness for $H \leq 22$).

trated in Figure 9, where only requiring a single night of pairs or requiring 6 observations in any sequence over 60 nights increases completeness over 10%. Pushing to SNR=4 requires substantial compute resources and is not cost effective in comparison.

When an NEO population is used instead of a PHA input population, the cumulative completeness is about 5% lower (see Figure 8). This is primarily due to differences in their

orbital distributions, as illustrated in Figure 3. The definition of PHAs includes a Minimum Orbit Intersection Distance (MOID) with Earth of 0.05 AU, requiring PHAs to more closely approach Earth than NEOs (which are defined as simply having $q < 1.3$ AU), and thus the PHAs achieve brighter peak V magnitudes than the NEOs. To quantify this effect, we calculated the apparent V magnitude for both the NEO and PHA input populations every night for ten years, while accounting for trailing losses and assuming a constant $H = 22$ magnitude for every member of the population. The resulting distributions of the brightest 10-year V magnitude values are shifted by about 0.3 magnitudes (the mean brightest magnitude values are 22.6 for NEOs and 22.3 for PHAs).

5.3.2. The Performance of Modified Surveys

The potential improvement in PHA discovery rates for modified survey cadences is summarized in the rows of Table 2 and described below.

- **Extra ecliptic spur visits:** By adding these extra visits over the course of a 10 year survey, the increase in completeness over the LSST baseline is only about 1%. This improvement comes at a cost to other science cases, as the main survey footprint (the WFD proposal) only receives 1,715,354 visits (82%) of the number of visits in the reference run; the outcome of many science programs is roughly proportional to the number of visits.
- **Extending the survey by two years:** Since `minion_1016` is a reference run, it only simulates 10 years. However, we can evaluate the “extra ecliptic visits” run at the 12 year mark, at which point the WFD proposal has received approximately the same number of visits as it would receive in the baseline 10 year survey. The additional two years of operations boost the completeness by about 4%.
- **Longer visits in the ecliptic:** This strategy reaches fainter limiting magnitudes, but the effect of longer exposures alone is minimized by the fact that trailing losses are also increased. It is also hard to disentangle the effects of increasing the visit time near the Ecliptic and the resulting lower frequency of observations (and thus fewer opportunities for sets of observations matching the basic discovery criteria). The small modifications made by this survey strategy actually show a decrease in completeness, *until* detection losses are partially compensated for by modifying source detection algorithms to the trailing loss level; then this run provides a similar completeness level as the “extra ecliptic visits” survey at twelve years. Presumably this is where modifying the observing strategy to favor large contiguous chunks of sky would make a significant

difference, consolidating the fewer ecliptic visits into a shorter amount of time suitable for object discovery.

- **Aggressively NEO-focused survey:** This survey uses a limited filter set, discards other proposals, and uses longer exposures along the ecliptic. This survey shows a modest increase in completeness (about 1.5%) relative to the “extra ecliptic visits” survey, after using longer MOPS windows and pushing source detection to the trailing loss level. However, many science programs would be jeopardized with this observing strategy because observations in the *uzy* filters, and observations of the DD and SCP fields, would not be obtained.

To summarize, when altering the survey strategy the largest individual gain ($\sim 4\%$) comes from simply extending the survey lifetime from 10 to 12 years. For the case of PHAs and 30-day wide MOPS window, the completeness can be boosted from 65.6% after 10 years with `minion_1016` survey to 73.9% after 12 years with “extra ecliptic visits” survey (recall that this completeness estimates do not account for the contribution of known objects).

5.4. The Impact of Objects Known Prior to LSST Survey

The completeness results presented above assumed that no objects are known prior to LSST survey. By including known objects, the completeness is boosted to higher values; the current (2016) completeness for NEOs with $H < 22$ is estimated to be about 25% (Grav et al. 2016). According to the JPL NEO discovery page¹⁰, one can conservatively estimate that discovery of 140m NEOs started in earnest in 2000.

We use a simplified model to estimate the contribution of known objects: since we do not know the survey pointing history for all the previous surveys, we simulate them by adopting a simple solar elongation cut and a two-step Johnson V magnitude threshold: V_{max1} before 2015 and V_{max2} after 2015, when several more sensitive surveys such as PanSTARRS started reporting NEO discoveries. We set the solar elongation cut to be 60° , roughly matching most telescope pointing capabilities, and assume V_{max2} (the limiting magnitude after 2015) to be 22.0, corresponding to the limiting magnitude expected from current state of the art surveys such as Pan-STARRS1. We integrate orbits for our synthetic NEO model population from 2000 to 2032 and consider an object discovered if its peak V magnitude is brighter than V_{max1} (before 2015) or V_{max2} (after 2015) while its solar elongation is greater than 60° . To

¹⁰See <http://neo.jpl.nasa.gov/stats/>

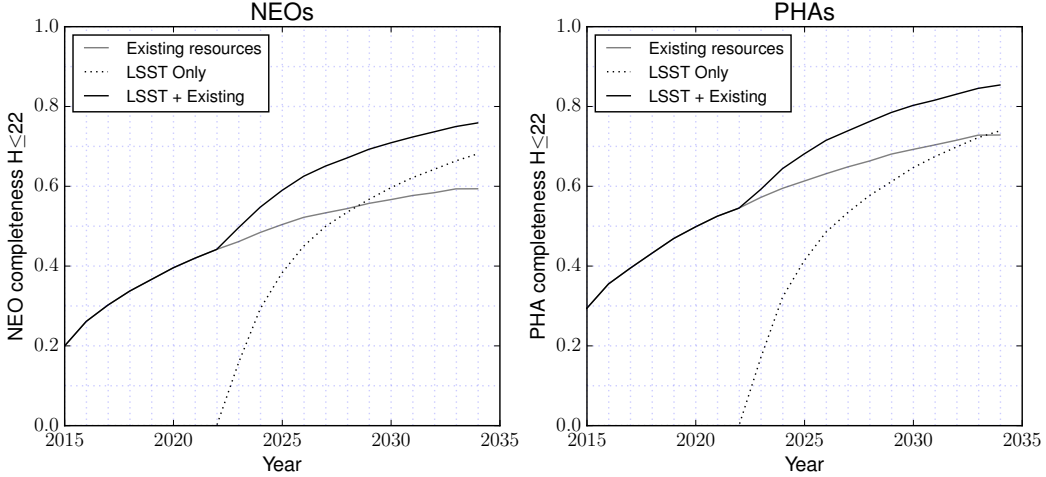


Fig. 10.— The cumulative completeness for NEOs (left) and PHAs (right) with $H \leq 22$, as a function of time, when known objects (gray solid lines) are taken (black solid lines) and not taken (dotted lines) into account (see also Table 3).

determine V_{max1} , we vary this threshold until the completeness for NEOs with $H < 22$ in 2016 is $\sim 25\%$, obtaining $V_{max1}=20.0$. This also produces a completeness of 95% for NEOs with $H < 18$ in 2015, i.e. for canonical objects larger than 1 km. With these conditions, we expect a 44% completeness for NEOs and 55% completeness for PHAs with $H < 22$ in 2022 at the start of the LSST survey. To determine the total impact of other surveys on LSST completeness, we continue discovering objects with $V_{max} = 22.0$ throughout the LSST survey; all objects discovered by these other surveys are added to the post-LSST sample, providing a boost to the final completeness of 8-11% for NEOs and 11-15% for PHAs.

Our results are summarized in Figure 10 and Table 3. For a 12-year survey, we predict a completeness of 85% for PHAs, when known objects are taken into account.

5.5. Systematic Effects due to Varying Modeling Assumptions

As indicated by the above discussion, a number of systematic effects must be taken into account when comparing different simulations of the same survey, as well as simulations of different surveys and observing systems. It is unlikely that a meaningful quantitative comparison can be pushed beyond a level of a few percent in completeness (in practice, the completeness of a given operating survey is best estimated using the object re-discovery rate). Based on our analysis, the leading systematic effects in simulated completeness estimates are:

1. NEO vs. PHA difference. The completeness is about $\sim 5\%$ higher for PHAs than for NEOs; for example, the cumulative completeness for `minion_1016` is 65.6% for PHAs and 60.7% for NEOs with 15 day MOPS windows.
2. Orbital parameter distribution for the simulated asteroid population (e.g. the Bottke model vs. the Granvik model); varying populations contribute completeness uncertainty of about a few percent).
3. Different sample definitions: $H < 22$ vs. $D > 140\text{m}$ (as shown by Grav et al. 2016, completeness increases by $\sim 5\%$ when an H -based criterion is used).
4. Variations of the “discovery window” (e.g., X visit pairs in N_w nights: changing N_w from 15 to 30 with X=3 increases completeness by about 3%, while changing N_w from 15 to 12 decreases completeness by about 1%).
5. Uncertainties when predicting effective image depth (system throughput, variation of the detection efficiency with the signal-to-noise ratio, treatment of trailing losses); for a survey that has a completeness above 60%, each additional *0.1 magnitude of depth for a given survey cadence increases the completeness by another 1%*.
6. Uncertainties when predicting asteroid’s apparent flux (albedo distribution, phase effects, photometric variability due to non-spherical shapes, color distributions); assuming an uncertainty of 0.2 mag in the effective limiting magnitude, the corresponding systematic uncertainty in completeness is about 2%.
7. Variations of the nominal detection threshold. If the detection threshold is changed from the signal-to-noise ratio of 5 or greater to 4 or greater, the completeness is boosted by $\sim 3\%$; the difference between the optimal detection using trailed profile and point-spread-function detection, which is negligible for LSST baseline exposure time of 30 seconds, would be worth $\sim 2\%$ in completeness for visits with a doubled exposure time.
8. Sensitivity to details in sky coverage and cadence (e.g. nightly pairs of visits vs. quads of visits). Requiring quads instead of pairs of visits decreases completeness by 30% using the baseline cadence; about half of that loss can be recovered using cadence simulations that request four visits per night.
9. The slope of the asteroid size distribution. Current measurement uncertainty of this parameter corresponds to a systematic uncertainty in completeness of about 2%.
10. The impact of known objects. We estimated that 55% of PHAs with $H < 22$ would be discovered by current survey assets by the start of LSST survey in 2022 (currently

~36%), and they would boost the final PHA completeness for 10-year LSST baseline survey by 14% (to 82.8%).

We proceed with an example of a comparison of different simulations.

5.6. A Comparison with the Grav, Mainzer & Spahr (2016) Study

Grav, Mainzer, & Spahr (2016, hereafter GMS) reported somewhat different NEO completeness levels than published by the LSST team in 2007 and 2014. Given the above discussion of various systematic effects, it is easy to understand the reported differences. There are three main reasons why the GMS results differ:

1. GMS *redefined* the completeness limit from the commonly used $H < 22$ criterion to an albedo-dependent value of H limit (which attempts to directly model the $D > 140$ m size limit).
2. GMS used a different realization of the LSST baseline survey.
3. GMS used a different realization of the PHA population.

The first of these effects is the dominant one. Redefining the completeness limit from $H < 22$ to $D > 140$ m leads to a drop in completeness of about 5% according to GMS (*i.e.* GMS would calculate a completeness of about 5% less for NEOs and PHAs). Different versions of the simulated survey include advances in our understanding of the system throughput and delivered seeing. For example, between *enigma_1189* (the baseline simulated survey used in GMS) and the new baseline *minion_1016* used here, the limiting magnitudes are on average a few tenths of a magnitude fainter in *enigma_1189* due to changes in the system throughput and delivered seeing; as a result, the completeness values are about 2% larger for *enigma_1189* than for *minion_1016*. These two surveys are statistically the same otherwise. For the NEO population, both GMS and this work used samples from the Grav et al. (2011) model and calculate similar results for completeness (after adjusting for the other two effects).

In summary, the GMS calculation of 62% completeness for PHAs (12-day window and $D > 140$ m) corresponds well to our 65.6% completeness (see Table 2) for PHAs with $H < 22$ (15-day window). Therefore, after accounting for different choices of simulation parameters, we conclude the GMS results are fully consistent (within 1-2 %) with the results previously published by the LSST team, as well as with the results discussed here.

Table 3. The cumulative completeness (in %) for NEOs and PHAs with $H \leq 22$ for LSST baseline survey strategy extended to a 12-year survey (with some extra visits along the Ecliptic, corresponding to the second row in Table 2). The length of track linking window (N_w) is set to 30 days, and the detection threshold is set to SNR= 5.

Population	10 year survey		12 year survey	
	only LSST	w/ known	only LSST	w/ known
NEO	63.5	73.9	68.1	75.9
PHA	68.4	82.8	73.9	85.4

6. Discussion and Conclusions

We have discussed here the ability of LSST to contribute to Near-Earth Objects (NEO) discoveries and the Congressional George E. Brown, Jr. mandate to NASA. We have quantitatively addressed the robustness of the LSST strategy for discovering NEOs using nightly pairs of observations, and the expected cumulative completeness for PHAs with $H < 22$.

We argued that the observing and data processing strategies chosen by LSST are robust. The robust determination of false positive detection rate in difference images presented here is based on data obtained with DECam and processed using prototype LSST software. Assuming the same rate, numerical tests with MOPS demonstrate that even a modest compute system will be adequate to process LSST data. Even if the false positive detection rate in difference images is twice as high as reported here, it can still be handled without a change of baseline cadence, linking criteria, or increase of computing resources. Quantitatively, the false positive rates of up to about 1000 deg^{-2} could be readily handled with an approximately 1000-core machine dedicated for moving object processing.

There is a significant compute margin, both because LSST compute needs are driven by other more demanding processing, and because there are various mitigation strategies that can decrease the compute load. For example, minor modifications of cadence, such as a simple shortening of the nightly revisit time by about a factor of 3, could mitigate about a factor of two increase in the false positive detection rate. At the same time, several times larger false positive rates for LSST than measured using DECam images and prototype LSST software are rather implausible. If the LSST camera, or any other system component, would somehow cause such high false positive rates, the whole LSST mission would be jeopardized.

In summary, the LSST strategy for discovering moving Solar System objects will be successful because the following three conditions will be met:

1. The LSST system hardware and image differencing software performance will result in false positive rates not significantly exceeding $\rho_{FP} = 400 \text{ deg}^{-2}$, estimated here using DECam data and prototype LSST software.
2. Given an anticipated 1000-core machine, MOPS will be able to easily process as many as 10^8 tracklets per search window, and daily computations to produce up to about 10^7 candidate tracks will be completed in about an hour.
3. Assuming that IOD can be executed in about 0.1 sec per track, this final filtering step can be easily accomplished in about an hour.

Our results show that the current LSST baseline survey strategy would yield a complete-

ness for PHAs with $H < 22$ of about 68% (without including known objects). We discuss a number of systematic effects that must be taken into account when comparing different simulations of the same survey, as well as simulations of different surveys and observing systems. The largest effect, at the level of 5%, is due to orbital differences between NEO and PHA populations. We compared our results presented here, as well as our previously published and consistent results, to an analogous recent study by Grav et al. (2016). We found that purported discrepancies can be fully understood as due to various systematic effects discussed in §5.5. All these recent results are by and large consistent within modeling uncertainties with even the earliest forecasts of LSST performance (e.g., the 10-year LSST baseline cadence would result in 75% completeness for PHAs with $H < 22$, according to Ivezić et al. 2007).

We describe a number of modifications of the LSST baseline survey which potentially could raise the completeness for PHAs with $H < 22$ beyond 80%. In particular, the “extra ecliptic visits” survey (astro_lsst_01_1016) can boost the completeness to 85% with a 12-year survey and known objects accounted for. In this cadence, the main LSST survey (“deep-wide-fast”) receives as many visits after 12 years as it would receive after 10 years of the baseline cadence (minion_1016). Therefore, most of other science programs would retain their performance if the “extra ecliptic visits” survey was adopted for LSST, and resources identified to prolong the survey from 10 years to 12 years. With substantial additional investment in data processing to enable detecting to $SNR = 4$ level and improved trailed source detections, the completeness could be further pushed to about 88%.

This material is based upon work supported in part by the National Science Foundation through Cooperative Agreement 1258333 managed by the Association of Universities for Research in Astronomy (AURA), and the Department of Energy under Contract No. DE-AC02-76SF00515 with the SLAC National Accelerator Laboratory. Additional LSST funding comes from private donations, grants to universities, and in-kind support from LSSTC Institutional Members.

A. LSST Image Processing Steps and Data Products Relevant for Asteroids

The data products produced by the LSST Data Management system are described in LSST Document LSE-163 (LSST Data Products Definition Document, Jurić et al. 2016). Here we briefly summarize parts of that document¹¹ that are most relevant for discovering moving Solar System objects.

The LSST Data Management system will perform nightly analysis of difference images¹², with the goal of detecting and characterizing astrophysical phenomena revealed by their time-dependent nature. The detection of supernovae superimposed on bright extended galaxies is an example of this analysis, and, of course, moving Solar System objects are another example. The processing will be done on a nightly/daily basis and will result in the so-called Level 1 data products. Level 1 products will include difference images, catalogs of sources detected in difference images (the so-called **DIASources**), static astrophysical objects¹³ these **DIASources** are positionally associated to (the so-called **DIAObjects**), and moving Solar System objects (**SSObjects**¹⁴). The catalogs will be entered into the Level 1 database and made available in near real time. Notifications (“alerts”) about new **DIASources** will be issued using community-accepted standards¹⁵ within 60 seconds of observation.

The Moving Object Processing System (**MOPS**) pipeline combines all unassociated **DIASources** into plausible **SSObjects** and estimates their orbital parameters. The three main pipeline stages include associating new **DIASources** with known **SSObjects**, discovering new **SSObjects**, and orbit refinement and management. This conceptual MOPS design is illustrated in Figure 11. Further details about the MOPS pipeline design and implementation are available from the LSST Science Pipelines Design Document (Jurić et al. 2013). The next section briefly describes the main processing steps in the nightly/daily Level 1 data processing.

¹¹To ensure the continued scientific adequacy of LSST data products, their designs and plans are periodically reviewed and updated and thus LSE-163 is a living document – please always consult the latest version.

¹²A difference image is an image produced by subtracting a science image from an appropriate “average” of the previously collected similar images of the same sky area, and using the same filter.

¹³The LSST has adopted the nomenclature by which single-epoch detections of astrophysical *objects* are called *sources*. The reader is cautioned that this nomenclature is not universal: some surveys call *detections* what LSST calls *sources*, and use the term *sources* for what LSST calls *objects*.

¹⁴**SSObjects** used to be called “Moving Objects” in previous versions of the LSST Data Products baseline. The name is potentially confusing as high-proper motion stars are moving objects as well. A more accurate distinction is the one between objects *inside* and *outside* of the Solar System.

¹⁵For example, VOEvent, see <http://ls.st/4tt>

8 Moving Object Processing System

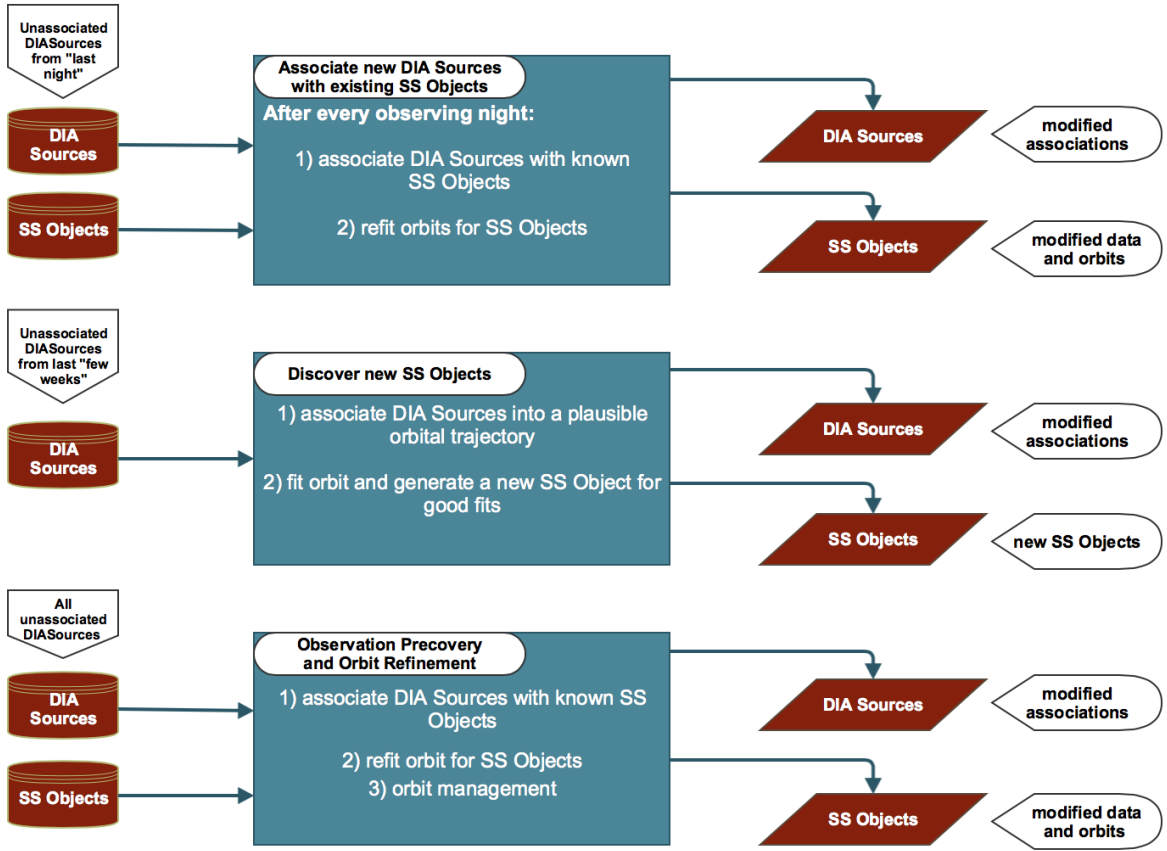


Fig. 11.— Illustration of the conceptual algorithm design for the Moving Object Processing System. **DIASources** are data structures that describe detections of sources in difference images and **SSObjects** are data structures that describe discovered Solar System objects (see Table A.1.4).

A.1. LSST Level 1 Data Processing

Level 1 data products are a result of difference image analysis (DIA). **DIASources** are sources detected on difference images with the signal-to-noise ratio $S/N > transSNR$, with $transSNR=5$. They represent changes in flux with respect to a deep template. Physically, a **DIASource** may be an observation of new astrophysical object that was not present at that position in the template image (for example, an asteroid), or an observation of flux change in an existing source (for example, a variable star). The flux can be negative (eg., if a source present in the template image reduced its brightness, or moved away). The shape can be complex (eg., trailed, for a source with proper motion approaching $\sim \text{deg/day}$, or “dipole-

like”, if an object’s observed position exhibits an offset – true or apparent – compared to its position on the template). Some **DIASources** will be caused by background fluctuations; with $transSNR = 5$, the expected false positive rate is about three per CCD (~ 60 per sq. deg.) for the median seeing, or of the order 500,000 per typical night. The expected number of false positives due to background fluctuations is a very strong function of adopted $transSNR$: a change of $transSNR$ by 0.5 results in a variation of an order of magnitude, and a change of $transSNR$ by unity changes the number of false positives by about two orders of magnitude (see Section 3.2).

Clusters of **DIASources** detected on visits taken at different times are associated with either a **DIAObject** or an **SSObject**, to represent the underlying astrophysical phenomenon. The association can be made in two different ways: by assuming the underlying phenomenon is an object within the Solar System moving on an orbit around the Sun¹⁶, or by assuming it to be distant enough to only exhibit small parallactic and proper motion¹⁷. The latter type of association is performed during difference image analysis right after the image has been acquired. The former is done at daytime by **MOPS**, unless the **DIASource** is an apparition of an already known **SSObject**. In that case, it will be flagged as such during difference image analysis. At the end of the difference image analysis of each visit, LSST will issue time domain event alerts for all newly detected **DIASources**¹⁸.

A.1.1. Nightly Difference Image Processing

The following is a high-level description of steps which will occur during regular *nightly* difference image analysis:

1. A visit is acquired and reduced to a single *visit image* (cosmic ray rejection, instrumental signature removal¹⁹, etc.).
2. The visit image is differenced against the appropriate template and **DIASources** are

¹⁶LSST pipelines will not fit for motion around other Solar System bodies; eg., identifying new satellites of Jupiter is left to the community.

¹⁷Where “small” is small enough to unambiguously positionally associate together individual apparitions of the object.

¹⁸For observations on the Ecliptic near the opposition Solar System objects will dominate the **DIASource** counts and (until they’re recognized as such) overwhelm the explosive transient signal. It will therefore be advantageous to quickly identify the majority of Solar System objects early in the survey.

¹⁹Eg., subtraction of bias and dark frames, flat fielding, bad pixel/column interpolation, etc.

detected and their properties measured.

3. The flux and shape²⁰ of the **DIA****Source** are measured on the difference image. PSF photometry is performed on the visit image at the position of the **DIA****Source** to obtain a measure of the total flux.
4. The Level 1 database is searched for a **DIA****Object** or an **SSO****bject** with which to positionally associate the newly discovered **DIA****Source**²¹. If no match is found, a new **DIA****Object** is created and the observed **DIA****Source** is associated to it.
5. If the **DIA****Source** has been associated with an **SSO****bject** (a known Solar System object), it will be flagged as such and an alert will be issued. Further processing will occur in daytime (see §A.1.2 below).
6. Otherwise, the associated **DIA****Object** measurements will be updated with new data collected during previous 12 months. All affected columns will be recomputed, including proper motions, centroids, light curves, etc.
7. The Level 2 database²² is searched for **Objects** positionally close to the **DIA****Object**, returning the three nearest stars and three nearest galaxies. The IDs of these nearest-neighbor **Objects** are recorded in the **DIA****Object** record and provided in the issued event alert.
8. An alert is issued that includes the **DIA****Source** ID, the **SSO****bject** ID or **DIA****Object** ID, and the associated science content (centroid, fluxes, low-order lightcurve moments, periods, etc.), including the full light curves.
9. For all **DIA****Objects** overlapping the field of view, including those that have an associated new **DIA****Source** from this visit, forced photometry will be performed on difference image (point source photometry only). No alerts will be issued for these **DIA****Sources**.
10. Within 24 hours of discovery, *precovery* PSF forced photometry will be performed on any difference image overlapping the position of new **DIA****Objects** taken within the

²⁰The “shape” in this context consists of weighted 2nd moments of the intensity distribution, as well as fits to a trailed source model and a dipole model.

²¹The association algorithm will guarantee that a **DIA****Source** is associated with not more than one existing **DIA****Object** or **SSO****bject**. The algorithm will take into account the parallax and proper (or Keplerian) motions, as well as the errors in estimated positions of **DIA****Object**, **SSO****bject**, and **DIA****Source**, to find the maximally likely match. Multiple **DIA****Sources** in the same visit will not be matched to the same **DIA****Object**.

²²Level 2 database is a database resulting from annual data release processing.

past 30 days, and added to the database. Alerts will not be issued with precovery photometry information.

In addition to the processing described above, a smaller sample of sources detected on difference images *below* the nominal $transSNR = 5$ threshold will be measured and stored, in order to enable monitoring of difference image analysis quality.

Also, the system will have the ability to measure and alert on a limited²³ number of sources detected below the nominal threshold for which additional criteria are satisfied. For example, a $transSNR = 3$ source detection near a gravitational keyhole²⁴ may be highly significant in assessing the danger posed by a potentially hazardous asteroid. The initial set of criteria will be defined by the start of LSST operations.

A.1.2. Solar System Object Processing

The following will occur during regular Solar System object processing in daytime²⁵, after a night of observing (see Figure 11):

1. The orbits and physical properties of all **SSObjects** re-observed on the previous night are recomputed. External orbit catalogs (or observations) are also used to improve orbit estimates. Updated data are entered to the **SSObjects** table.
2. All **DIASources** detected on the previous night, that have *not* been matched at a high confidence level to a known **Object**, **DIAObject**, **SSObject**, or an artifact, are analyzed for potential pairs, forming *tracklets*.
3. The collection of tracklets collected over the past 30 days is searched for subsets forming *tracks* consistent with being on the same Keplerian orbit around the Sun.
4. For those that are, an orbit is fitted and a new **SSObject** table entry created. **DIASource**

²³It will be sized for no less than $\sim 10\%$ of average **DIASource** per visit rate.

²⁴A gravitational keyhole is a region of space where Earth’s gravity would modify the orbit of a passing asteroid such that the asteroid would collide with the Earth in the future.

²⁵Note that there *is no strict bound on when daytime Solar System processing must finish*, just that, averaged over some reasonable timescale (eg., a month), a night’s worth of observing is processed within 24 hours. Nights rich in moving objects may take longer to process, while nights with less will finish more quickly. In other words, the system requirement is on *throughput*, not latency.

records are updated to point to the new `SSObject` record. `DIAObjects` “orphaned” by this unlinking are deleted.²⁶.

5. Precovery linking is attempted for all `SSObjects` whose orbits were updated in this process. Where successful, `SSObjects` (orbits) are recomputed as needed.

A.1.3. Level 1 Catalogs

The described alert processing design relies on the “living” Level 1 database that contains the objects and sources detected on difference images. At the very least²⁷, this database will have tables of `DIASources`, `DIAObjects`, and `SSObjects`, populated in the course of nightly and daily difference image and Solar System object processing²⁸. As these get updated and added to, their updated contents becomes visible (queryable) immediately²⁹.

Table A.1.4 presents the *conceptual schema* for the `SSObject` table (it conveys *what* data will be recorded in each table, rather than the details of *how*). Columns whose type is an array will likely be expanded to one table column per element of the array once this schema is translated to SQL³⁰. In addition, the table presented here is normalized (i.e., it contains no redundant information with other tables in Level 1 database). For example, since the band of observation can be found by joining a `DIASource` table to the table with exposure metadata, there’s no column named `band` in the `DIASource` table. In the as-built database, the views presented to the users will be appropriately denormalized for ease of use.

A.1.4. `SSObject` Table

Name	Type	Unit	Description
<code>ssObjectId</code>	uint64		Unique identifier.

Continued on next page

²⁶Some `DIAObjects` may only be left with forced photometry measurements at their location (since all `DIAObjects` are force-photometered on previous and subsequent visits); these will be kept but flagged as such.

²⁷It will also contain exposure and visit metadata, MOPS-specific tables, etc.

²⁸The latter is also colloquially known as *DayMOPS*.

²⁹No later than the moment of issuance of any event alert that may refer to it.

³⁰The SQL realization of this schema can be browsed at <http://ls.st/8g4>

Name	Type	Unit	Description
oe	double[7]	various	Osculating orbital elements at epoch (q , e , i , Ω , ω , M_0 , epoch).
oeCov	double[21]	various	Covariance matrix for oe.
arc	float	days	Arc of observation.
orbFitLnL	float		Natural log of the likelihood of the orbital elements fit.
orbFitChi2	float		χ^2 statistic of the orbital elements fit.
orbFitNdata	int		The number of data points (observations) used to fit the orbital elements.
MOID	float[2]	AU	Minimum orbit intersection distances ³¹
moidLon	double[2]	degrees	MOID longitudes.
H	float[6]	mag	Mean absolute magnitude, per band (Muinonen et al. 2010 magnitude-phase system).
G ₁	float[6]	mag	G_1 slope parameter, per band (Muinonen et al. 2010 magnitude-phase system).
G ₂	float[6]	mag	G_2 slope parameter, per band (Muinonen et al. 2010 magnitude-phase system).
hErr	float[6]	mag	Uncertainty of H estimate.
g1Err	float[6]	mag	Uncertainty of G_1 estimate.
g2Err	float[6]	mag	Uncertainty of G_2 estimate.
flags	bit[64]	bit	Various useful flags.

The G_1 and G_2 parameters for the large majority of asteroids will not be well constrained until later in the survey. LSST may decide not to fit for it at all over the first few DRs and

³¹<http://www2.lowell.edu/users/elgb/moid.html>

add it later in Operations, or provide two-parameter G_{12} fits. Alternatively, they may be fitted using strong priors on slopes poorly constrained by the data. The design of the data management system is insensitive to this decision, making it possible to postpone it to Commissioning to ensure it follows the standard community practice at that time. The LSST database will provide functions to compute the phase (Sun-Asteroid-Earth) angle α for every observation, as well as the reduced, $H(\alpha)$, and absolute, H , asteroid magnitudes in LSST bands.

B. The Impact of False Positives on MOPS Performance

We seek to develop an analytic understanding for the behavior of the MOPS results. In particular, we want to be able to predict the numbers of tracklets and candidate tracks for a given input number of true and false detections. In addition, we seek to understand how these numbers scale with the search window width, velocity cutoff when forming tracklets, the temporal separation of two detections in a tracklet, and the density of false positives. For example, available MOPS experiments indicate that the number of tracklets increases with the square of the false positives density, but other scalings are unclear, especially the behavior of false candidate tracks.

We first derive the simpler false tracklet rates, and then use these results to discuss false candidate track rates.

B.1. Expected False Tracklet Rates

Given a detection in the first difference image, another difference image, obtained at a different epoch, is searched for a matching detection to form a tracklet. For orientation, the sky density of asteroids down to LSST 5σ faint flux limit ($r \sim 24.5$) is of the order $\rho_{ast} \sim 100 \text{ deg}^{-2}$. The predicted highest asteroid sky density for $r < 24.5$, on the Ecliptic, is up to about five times larger (with an uncertainty of about a factor of 2, depending on model assumptions), and the density decreases rapidly with the ecliptic latitude. A typical LSST observing night includes about 1000 visits, with two visits per night over the active sky area. The nominal LSST field-of-view area is $A_{FOV} = 9.6 \text{ deg}^2$, with a fill factor of 0.9, giving an effective field-of-view area of $A_{FOV}^{eff} = 8.64 \text{ deg}^2$. Hence, the number of detected asteroids per night is of the order 500,000 (with implied two detections per asteroid), although it can be significantly lower when the Ecliptic is not well covered (and it could be a few times higher if the majority of visits were obtained along the Ecliptic).

The number of false detections due to (Gaussian) background fluctuations is about $\rho_{bkgd} = 60 \text{ deg}^{-2}$, assuming typical LSST seeing (0.8 arcsec) and SNR>5. For a given seeing and SNR threshold, the rate of false positives can never be lower than this estimate. This false positive rate decreases with the square of the seeing, and strongly depends on SNR: the rate increases/decreases by as much as a factor of about ten when SNR threshold is changed to 4.5 and 5.5, respectively (see §3).

Analysis of DECam images reduced using prototype LSST software, described in §3, shows a higher rate of detections in difference images, and a fraction of those detections cannot be readily associated with true moving objects. This analysis implies a conservative

upper limit for the false positive rate of about $\rho_{FP} = 400 \text{ deg}^{-2}$. This value is conservative because analyzed DECam fields are close to the Ecliptic, with a significant but not well known contribution from real asteroids (due to very faint flux levels, $r \sim 24$), and it also includes true astrophysical transients that are not associated with static objects (stars and galaxies). It is quite possible that the false positive rate might be several times lower, though we will proceed with the most conservative estimate above.

The sky density of detections in difference images, ρ_{det} , is given by the sum of contributions from true asteroids and false positives, $\rho_{det} = \rho_{ast} + \rho_{FP} = 500 \text{ deg}^{-2}$. When searching for a matching detection in another difference image, there are two distinct types of behavior. Correct matches of detections of the same asteroids into tracklets follow the behavior expected for correlated samples: as long as the object’s angular displacement between the two epochs is sufficiently larger than the seeing disk, while at the same time smaller than the search radius, the number of matches (that is, the number of true tracklets produced per LSST pointing, assuming two visits of the same area per night) is simply

$$N_{\text{tracklet}}^{\text{true}} = \rho_{ast} A_{FOV}^{\text{eff}}, \quad (\text{B1})$$

With $\rho_{ast} = 100 \text{ deg}^{-2}$, $N_{\text{tracklet}}^{\text{true}} \sim 1,000$ per a pair of visits, and with 500 visit pairs per typical observing night, $N_{\text{tracklet}}^{\text{true}} \sim 500,000$ per night (same as the number of detected asteroids in the active sky area, of course). Again, this number can be much lower for fields far away from the Ecliptic, and a few times larger for exceptionally good coverage of the Ecliptic. We emphasize that this number of true tracklets does not directly depend on the search radius, nor the time elapsed between the two visits, as long as they have their plausible values (about an arcminute, and a few tens of minutes, as discussed further below).

There are three other types of tracklets that follow behavior for uncorrelated (random) samples: associations of different asteroids, associations of asteroids and false detections, and tracklets made of two false detections. Assuming the same ρ_{det} in both difference images, for each of $N_{\text{det}} = \rho_{det} A_{FOV}^{\text{eff}}$ detections in one image, we search for a matching detection in another image (see Figure 12). The search radius is given by

$$\delta_{max} = v_{max} \Delta t. \quad (\text{B2})$$

Here v_{max} is the cutoff velocity and Δt is the time elapsed between the two images. For LSST baseline cadence, Δt is in the range 20-60 minutes. The search area, $A_S = \pi \delta_{max}^2$, is then

$$A_S = 0.0055 \left(\frac{v_{max}}{\text{deg day}^{-1}} \right)^2 \left(\frac{\Delta t}{\text{hour}} \right)^2 \text{deg}^2. \quad (\text{B3})$$

To guide setting the cutoff velocity, simulations imply that 95% of NEO detections have $v < 1 \text{ deg day}^{-1}$; with this threshold, the completeness for main-belt asteroids is essentially

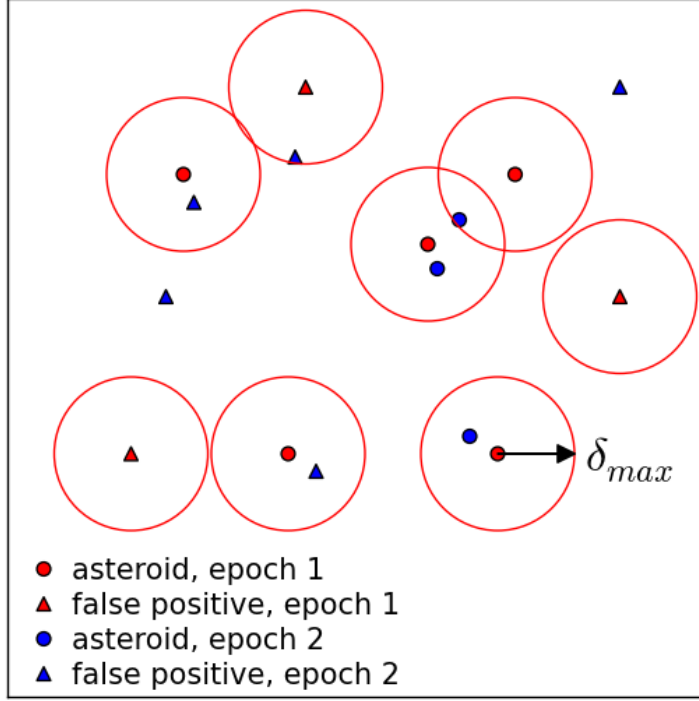


Fig. 12.— An illustration of positional matching of detections to form tracklets. Detections come in two flavors: asteroids (A, circles) and false positives (FP, triangles). The figure shows the search for a matching detection in epoch 2 for each detection in epoch 1, with a maximum search radius δ_{max} . Note that there are six possibilities: matches A-A, A-FP, FP-A, FP-FP, and orphaned A and FP.

100%. Objects moving faster than 1 deg day^{-1} will be easily resolved in LSST images and can be treated separately using specialized algorithms. Adopting $v_{max} = 1 \text{ deg day}^{-1}$, and $\Delta t = 30 \text{ minutes}$ (which together imply a search radius of $\delta_{max} = 1.3 \text{ arcmin}$), gives a search area of $A_S = 0.0014 \text{ deg}^2$.

The expectation value for the number of matching detections within the search area A_S (that is, the expected number of tracklets per matching trial) is

$$p_{\text{tracklet}}^{\text{false}} = \rho_{\text{det}} A_S, \quad (\text{B4})$$

and the total expected number of *false* tracklets for N_{det} trials is thus

$$N_{\text{tracklet}}^{\text{false}} = N_{\text{det}} p_{\text{tracklet}}^{\text{false}} = N_{\text{visit}} \rho_{\text{det}}^2 A_S A_{\text{FOV}}^{\text{eff}} = N_{\text{visit}} \rho_{\text{FP}}^2 A_S A_{\text{FOV}}^{\text{eff}} (1 + 2\eta + \eta^2), \quad (\text{B5})$$

where $\eta = \rho_{\text{ast}}/\rho_{\text{FP}} \sim 0.25$ (recall that $\rho_{\text{det}} = \rho_{\text{ast}} + \rho_{\text{FP}}$). With $\rho_{\text{ast}} = 100 \text{ deg}^{-2}$ and $\rho_{\text{FP}} = 400 \text{ deg}^{-2}$, $N_{\text{tracklet}}^{\text{false}} \sim 3,000$ per pair of visits, and $N_{\text{tracklet}}^{\text{false}} \sim 1.5 \text{ million}$ per observing night

with $N_{visit} = 500$ visit pairs. We note that the density of false tracklets ($\rho_{tracklet}^{false} = 350 \text{ deg}^{-2}$) is similar to ρ_{FP} ; this similarity is a consequence of choosing δ_{max} such that $\rho_{FPA_S} \sim 1$.

The first term in eq. B5 is the largest and corresponds to tracklets made of two false detections (~ 1.0 million), the second term corresponds to associations of asteroids and false detections, and the third and the smallest term (< 0.1 million) is due to incorrect associations of different asteroids. For the chosen parameter values, the total number of tracklets is about 2 million per observing night. Given that these choices are rather conservative, this estimate is essentially an upper limit; approximately, *we expect of the order a million tracklets per observing night.*

To the first order ($\eta \approx 0$), the total number of tracklets per night is

$$N_{tracklet} = N_{tracklet}^{true} + N_{tracklet}^{false} = N_{visit} A_{FOV}^{eff} (\rho_{ast} + \rho_{FP}^2 A_S). \quad (\text{B6})$$

In addition to $N_{tracklet}^{false}$ scaling with the square of ρ_{FP} , as demonstrated using MOPS, $N_{tracklet}^{false}$ scales with the square of both v_{max} and Δt (via the dependence on A_S). Therefore, if Δt would be made as small as 10 minutes by modifying observing strategy, the resulting $N_{tracklet}^{false}$ would be about an order of magnitude smaller (and $N_{tracklet}$ about three times smaller). Hence, the shortening of Δt is a good mitigation strategy against high false positive detection rates in difference images³².

B.1.1. False tracklet velocity distribution

False tracklets have randomly distributed velocities (motion vectors) with a cutoff given by v_{max} (recall that $v_{max} = 1 \text{ deg day}^{-1}$ was adopted above). The implied tracklet velocity is given by

$$v = \delta / \Delta t, \quad (\text{B7})$$

where δ is the angular separation of two detections. Since the number of tracklets with separation δ increases linearly with δ (because the area of a circular annulus is $2\pi r dr$), the false tracklet velocity distribution will increase linearly with v for $v < v_{max}$, and the vector orientation will be random. We show below that candidate tracks can be efficiently pruned using this result.

³²An extreme example of this mitigation strategy would be to obtain two consecutive 30-second visits – their mid-exposure times would be separated by 34 seconds (additional 2 seconds due to shutter motion and another 2 seconds due to readout), which is sufficient to detect motion faster than about 0.1 deg day^{-1} .

B.2. Expected False Track Rates

In this section, we present an approximate estimate of the expected number of false candidate tracks. Our goal is to derive the scaling of this number with relevant input parameters, such as the true and false tracklet rates per night ($N_{\text{tracklet}}^{\text{true}} = 5 \times 10^5$ and $N_{\text{tracklet}}^{\text{false}} = 1.5 \times 10^6$, respectively). For a fiducial case, we assume that the search window is $N_w = 30$ days wide; therefore, with $N_{\text{tracklet}} = 2 \times 10^6$ per night, there are 6×10^7 tracklets in the fiducial dataset. With about $4,300 \text{ deg}^2$ (500 pairs of visits) of sky observed each night, the average density of (all) tracklets is $\rho_{\text{tracklet}} = 450 \text{ deg}^{-2}$. Assuming that on average the same field is revisited every $T_{\text{revisit}} = 3$ days, the active area includes about $13,000 \text{ deg}^2$ of sky.

As discussed below in more detail, there are of the order 1000 different ways to chose a triplet of nights from the search window. Given 10^6 tracklets per night, there are of the order 10^{21} different combinations of tracklet triplets that could form a candidate track. While this number of candidate tracks is obviously prohibitively large to test for consistency with heliocentric Keplerian motion, it can be sufficiently reduced (to about the same number as the number of true tracks along the Ecliptic) using pre-filtering steps based on tracklet motion vectors, as follows.

In the first step, the motion vector of a tracklet from the first night is linearly extrapolated to the second night and tracklets from the second night are searched for within a radius set by the orbital curvature (which dominates over astrometric errors). With appropriate use of kd-tree and similar algorithms for fast searches, only a small fraction (of the order a percent) of tracklets from the second night need to be examined in detail. The cutoff radius varies from ~ 1 arcmin for the case of two consecutive nights to ~ 1 deg. for 15-day separation (as discussed in detail further below). In addition, the velocity of second tracklet is required to be consistent with the velocity implied by the positions of the two tracklets. After this step, there are about 10^{10} tracklet pairs for further processing (for $N_w = 30$ days).

In the second step, parameters of a parabola (for each coordinate) are constrained using the positions and velocities of the two tracklets, and this parabolic motion is extended to a third night to search for matching third tracklet. This step results in up to 10^{11} candidate tracks.

Using positions of the three tracklets, parabolic motion (for each coordinate) is fit in the third step. Velocities implied by this motion fit are compared to velocities for the first and third tracklet. This filtering step reduces the number of candidate tracks by a factor of about 10^{-5} and brings the number of false candidate tracks to the same range as the number of true tracks close to the Ecliptic. These three matching and pre-filtering steps bring the

number of candidate tracks to a level that can be easily handled by the IOD filtering step.

We now proceed with a more detailed description of three pre-filtering steps for candidate tracks.

B.2.1. The Number of 3-night Combinations in the Search Window

We can form a candidate triplet of tracklets by first choosing the middle (second) tracklet. For simplicity, we will measure time of observation in integer days. Given N_w nights in the search window, the middle tracklet comes from night indexed k , with $2 \leq k \leq (N_w - 1)$. The night that contributes the first tracklet is indexed by j , with $1 \leq j \leq (k - 1)$, and the night that contributes the third tracklet is indexed by l , with $(k + 1) \leq l \leq N_w$. The number of 3-night combinations can be expressed in a closed form

$$N_{3nights} = \sum_{k=2}^{N_w-1} (k-1)(N_w-k) = \frac{1}{6}N_w^3 - \frac{1}{2}N_w^2 + \frac{1}{3}N_w, \quad (\text{B8})$$

giving $N_{3nights} = 455$ for $N_w = 15$ and $N_{3nights} = 4,060$ for $N_w = 30$. Note that for large N_w , N_{3night} is proportional to N_w^3 – the number of 3-nights combinations increases by about an order of magnitude when N_w is doubled from 15 days to 30 days.

It is important to point out that in steady-state processing a single night is added to the window from the previous night, and the first night is dropped. Therefore, only the *new* 3-night combinations, where the third night is the last night in the search window, need be considered in steady-state processing (and the ramp up is easy because of gradually increasing search window size). It is straightforward to show that the number of such 3-night combinations is

$$N_{3nights}^{new} = \sum_{k=2}^{N_w-1} (k-1) = \frac{1}{2}N_w^2 - \frac{3}{2}N_w + 1, \quad (\text{B9})$$

yielding $N_{3nights}^{new} = 91$ for $N_w = 15$ and $N_{3nights}^{new} = 406$ for $N_w = 30$. Note that $N_{3nights}^{new} \sim N_{3nights}/10$ for $N_w = 30$, which represents a significant reduction.

B.2.2. The Tracklet Motion Vector Accuracy

In addition to its mean position at the mean epoch, each tracklet constrains the motion vector. Typical astrometric errors for LSST detections will range from about 50 mas at SNR=100 to 150 mas at SNR=5. For simplicity, we will assume hereafter that the astrometric

errors are $\sigma_a = 150$ mas for all detections, or ~ 100 mas per coordinate. With a temporal separation of two detections in a tracklet of Δt , the motion vector is measured with an accuracy per coordinate of

$$\sigma_v = 3.6 \left(\frac{\text{hour}}{\Delta t} \right) \text{ arcsec day}^{-1}. \quad (\text{B10})$$

With a typical $\Delta t = 30$ min, and assuming a linear motion in each ecliptic coordinate (longitude λ and latitude β), each coordinate can be predicted at time t with an accuracy of

$$\sigma_x = 7.2 \Delta k \text{ arcsec}, \quad (\text{B11})$$

where Δk , in days, is the elapsed time between the mean tracklet epoch and time t (for example, the number of nights between the first and the second tracklet in a candidate track). For illustration, when $\Delta k = 7$ days, $\sigma_x = 50$ arcsec, which is roughly the same as the typical detection separation in a tracklet, and comparable to typical distance between two tracklets. However, it turns out that positional discrepancies due to linear extrapolation of orbital motion for NEOs are an order of magnitude larger than the astrometric measurement errors even in case of two consecutive nights (~ 1 arcmin vs. 7 arcsec, respectively). We proceed with a quantitative analysis of required matching radius using simulated orbits for main-belt asteroids and NEOs.

B.2.3. Initial Linking of Tracklets into Candidate Tracks

Given a combination of 3 different nights from the search window, for each tracklet from the first night we can linearly extrapolate its motion vector and require that the measured position of a tracklet from the second night is consistent with the predicted position (the night ordering can be reversed from 1-2-3 to 3-2-1). Given a tracklet from the first night, it is not necessary to search through all tracklets from the second night. Search methods such as kd-trees can be used to rapidly reject tracklets that have no chance of being matched. As an example of a “poor man’s” rapid search, consider the fact that tracklets from each night are already “self-organized” into about 500 visits, which correspond to a field of view with a diameter of 3.5 deg. It is easy to show that with an upper limit on possible motion of 5 deg, only 19 visits from the second night need to be searched for matching tracklets. This significant reduction of a factor of ~ 25 in the number of candidate matching tracklets can be further boosted by applying more sophisticated tree algorithms.

Using for illustration ecliptic longitude λ , the predicted search position for the second tracklet is

$$\lambda_2^* = \lambda_1 + v_1^\lambda \Delta T_{21}, \quad (\text{B12})$$

where ΔT_{21} is the elapsed time between the epochs of the first and second tracklet, and v_1^λ is the longitudinal component of v_1 , the motion vector for the first tracklet, divided by $\cos(\beta)$. The expectation value for the number of matches in an ellipse (see the left panel in Figure 13) centered on predicted position (λ_2^*, β_2^*) , and within limits r_λ^{max} and r_β^{max} along the Ecliptic longitude and latitude, is given by

$$N_{match}(\Delta k) = \pi r_\lambda^{max} r_\beta^{max} \rho_{tracklet} \left(\frac{1 \text{ day}}{T_{revisit}} \right) \quad (\text{B13})$$

where division by $T_{revisit}$ reflects the fact that each field is revisited on average only every $T_{revisit}$ days (statistically speaking; the number of matches is zero for all but one night out of $T_{revisit}$ nights).

The extrapolation given by eq. B12 implies that orbits can be approximated by linear motion (in each coordinate) over time ΔT . This is an incorrect assumption due to orbital curvature and we analyze this effect using orbital simulations of MBA and NEO samples described in §5.1.1.

Analysis of simulated samples shows that an adequate acceleration limit³³ is $a^{max} = 0.02 \text{ deg day}^{-2}$: essentially all main-belt asteroids and more than 95% of NEOs satisfy this criterion. If acceleration were constant during an interval of Δk days, the maximum positional discrepancy would be proportional to Δk^2 . Numerical analysis of simulated orbital motions suggests that an approximately constant selection completeness (as a function of Δk) is attained for

$$r_\beta^{max} = A \Delta k^{1.5}. \quad (\text{B14})$$

with $A = 1.0 \text{ arcmin}$, and $r_\lambda^{max} = 5 r_\beta^{max}$. The achieved completeness for a fiducial $\Delta k=7$ days is 0.99 for MBAs and 0.95 for NEOs, with very little dependence on Δk for $1 \text{ day} \leq \Delta k \leq 21 \text{ days}$ (per single search window – note that most objects will have multiple discovery chances). With this linear motion model, the number of matched tracklets per single trial tracklet is

$$N_{match}^L(\Delta k) = 1.96 \left(\frac{1 \text{ day}}{T_{revisit}} \right) \left(\frac{\rho_{tracklet}}{450 \text{ deg}^{-2}} \right) (\Delta k)^3. \quad (\text{B15})$$

For example, the expected number of matches for $\Delta k=7$ days is ~ 224 (a 19 arcmin by 93 arcmin matching ellipse), and rises to $\sim 6,000$ for $\Delta k=21$ days.

Given the two matched tracklets, we approximate the motion as a parabola

$$\lambda(t) = \frac{1}{2} a^\lambda t^2 + v^\lambda t + \lambda_1, \quad (\text{B16})$$

³³See also Figure 16 in Myers et al. (2013)

where $t = mjd - mjd_1$ (and analogously for latitude β). Using the tracklet positions and the motion vector of the first tracklet, acceleration can be directly estimated as

$$a^\lambda = 2 \frac{\lambda_2 - \lambda_1 - v_1^\lambda \Delta T_{21}}{\Delta T_{21}^2}, \quad (\text{B17})$$

and the predicted velocity for the second tracklet can be estimated from

$$(v_2^\lambda)^* = a^\lambda \Delta T_{21} + v_1^\lambda = \frac{2(\lambda_2 - \lambda_1)}{\Delta T_{21}} - v_1^\lambda. \quad (\text{B18})$$

We find that a comparison of v_2^λ and $(v_2^\lambda)^*$ can further decrease the number of false tracks (recall §B.1.1); with tolerances of $\Delta v^\lambda < 0.3$ deg/day and $\Delta v^\beta < 0.07$ deg/day (applied simultaneously for both coordinates as an elliptical condition), the reduction is about a factor of 50 (for $v_{max} = 1$ deg day $^{-1}$), with only a minimal impact on the sample completeness. Therefore, depending on Δk , the number of tracklet pairs per trial tracklet to continue processing ranges from ~ 4 for $\Delta k=7$ days to ~ 120 for $\Delta k=21$ days. When added over all possible pairs of nights (with $T_{revisit} = 3$ days), the total number of candidate tracklet pairs normalized by the number of tracklets per night ranges from 350 for $N_w = 15$ days to 13,400 for $N_w = 30$ days. Therefore, the following, more involved, selection steps need to be executed for no more than about 10^{10} tracklet pairs (for $N_w = 30$ days; and only for 3×10^8 pair when $N_w = 15$ days). These numbers are significantly lower than the naive estimate of 10^{15} ($10^3 \times 10^6 \times 10^6$).

We note that in steady-state processing, the new candidate tracklet pairs need to be evaluated only for pairs of nights where the second night is the penultimate night in the search window (all other combinations will have been already computed on previous days). Because the caching of results from previous night is not yet implemented in MOPS, we don't account for this reduction (of about a factor of 3 to 6) in the analysis presented here.

Given the acceleration estimate from eq. B17, the position of the third tracklet can be predicted from

$$\lambda_3^* = \frac{1}{2} a^\lambda \Delta T_{32}^2 + v_2^\lambda \Delta T_{32} + \lambda_2. \quad (\text{B19})$$

Similarly to eq B14, an approximately constant selection completeness can be achieved using

$$r_\beta^{max} = B \Delta k^{1.5}. \quad (\text{B20})$$

with $B = 0.2$ arcmin, and $r_\lambda^{max} = 5 r_\beta^{max}$. Note that the search area is now 25 times smaller than in the first case, thanks to parabolic rather than linear extrapolation. Therefore, the number of matched tracklets per single trial tracklet pair is

$$N_{match}^P(\Delta k) = 0.078 \left(\frac{1 \text{ day}}{T_{revisit}} \right) \left(\frac{\rho_{tracklet}}{450 \text{ deg}^{-2}} \right) (\Delta k)^3, \quad (\text{B21})$$

and the expected number of matches ranges from 9 for $\Delta k=7$ days to ~ 240 for $\Delta k=21$ days.

The total number of candidate tracks per single trial tracklet, for all possible 3-night combinations (where the third night is the last night in the search window) is

$$N_{tracklet}^{tracks} = 3.2 \times 10^{-3} \left(\frac{\rho_{tracklet}}{450 \text{ deg}^{-2}} \right)^2 \left(\frac{1 \text{ day}}{T_{revisit}} \right)^2 \sum_{k=2}^{N_w-1} \sum_{j=1}^{k-1} (k-j)^3 (N_w - k)^3. \quad (\text{B22})$$

The normalization constant is equal to $1.96 \times 0.078 \times (\Delta v^\lambda \Delta v^\beta / v_{max}^2)$, where the term in parenthesis is ~ 0.02 . This normalization gives the number of candidate tracks per search window normalized by the number of tracklets per night (which is assumed constant for all nights). The two terms in the sum reflect the multiplication of the number of matches found in the first selection step (linear extrapolation from the first to the second night, eq. B15) and the number of matches found in the third selection step (parabolic extrapolation from the second to the third night, eq. B21).

The sums in eq. B22 can be evaluated analytically, but the result is cumbersome. Using numerical evaluation (with $T_{revisit} = 3$ days), we find that the number of candidate tracks per tracklet ranges from ~ 600 for $N_w = 15$ days to $\sim 174,000$ for $N_w = 30$ days ($N_{tracklet}^{tracks}$ scales with N_w^8 when the third night must be the last night from the search window). Therefore, the matching of the candidate third tracklet brings the number of candidate tracks per search window to the range $10^9 - 10^{11}$. The ratio of false candidate tracks to true tracks is in the range $10^3 - 10^5$, depending on N_w . Despite the reduction by a factor of about 10^{10} to 10^{12} from the combinatorial number of tracklet triplets, another significant reduction is required before the IOD step can be attempted.

B.2.4. Using Tracklet Motion Vectors to Prune Candidate Tracks

The positional matching described above didn't use strong constraints on tracklet velocities for the first and third tracklets. Since false tracklets have random velocities, velocity filtering can further reduce the number of false tracks. With three candidate tracklets, a parabolic motion (see eq. B16) can be fit *without* using tracklet velocities. This fit predicts velocity of each tracklet from the first derivative of the fit, which can then be compared to each measured velocity. Figure 13 illustrates a situation where, e.g., v_3 is inconsistent with velocity predicted using such parabolic fit.

The consistency tolerances are driven by orbital curvature and acceleration, rather than by velocity measurement errors (velocities are measured with a precision of about $0.001 \text{ deg day}^{-1}$, see eq. B10). Analysis of simulated samples described in §5.1.1 shows that velocity

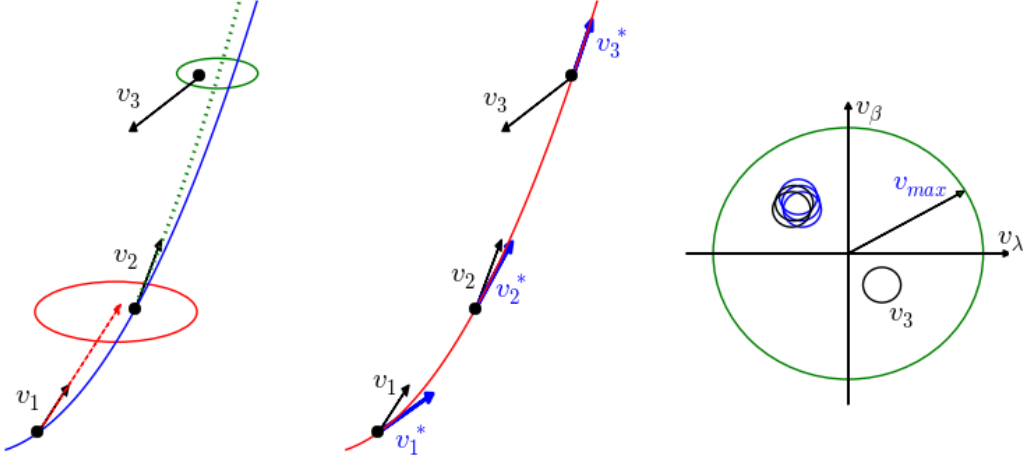


Fig. 13.— The left panel shows a hypothetical asteroid trajectory as the curved blue line (with the curvature greatly exaggerated). Three tracklets are shown by the black dots; the two individual detections per tracklet are not shown, but are implied by the three measured motion vectors (v_1 , v_2 and v_3). The third tracklet illustrates a false tracklet. The motion vector of the first tracklet is linearly extrapolated to the time of the second tracklet and matched within the red ellipse. The first two tracklets are then used to constrain parabolic extrapolation, shown by the green dotted line, which is then matched within the green ellipse. Given three candidate tracklets, a parabola is fit to their positions and predicted motion vectors are computed for each tracklet (the blue vectors in the middle panel). This comparison is illustrated in the right panel, where the circle signifies the cutoff velocity for forming tracklets. Note that the third tracklet has a measured velocity (v_3) that is inconsistent with the predicted velocity (v_3^*). The consistency radii are discussed in the text.

tolerances of $\delta v_{\lambda}^{max}=0.12 \text{ deg day}^{-1}$ for longitudinal component and $\delta v_{\beta}^{max}=0.03 \text{ deg day}^{-1}$ for latitudinal component reject most false tracklets with only a few percent effect (per single discovery attempt) on overall sample completeness.

The probability that a random false-tracklet velocity will be consistent with some true velocity is approximately (assuming a uniform distribution of false tracklet velocities)

$$p_v = \frac{\delta v_{\beta}^{max} \delta v_{\lambda}^{max}}{v_{max}^2} \quad (\text{B23})$$

With $v_{max} = 1 \text{ deg day}^{-1}$, $p_v = 0.0036$. In reality, this probability is a bit smaller because the false-tracklet velocity distribution is not uniform (it is biased towards the velocity cutoff). Finally, the probability that all three tracklets have velocities consistent with those implied

by their positions is $p_v^2 \sim 10^{-5}$ (not p_v^3 because v_2 was already subjected to a fairly stringent cut, see eq. B18; a more stringent cut here would provide a reduction by about a factor of five, which we ignore)

This significant reduction in the number of candidate false tracks, due to filtering velocities of the first and third tracklets, brings it to the range 10^4 - 10^6 , which is smaller or at most about the same as the number of true candidate tracks (on the Ecliptic). With this final reduction, the IOD step can be attempted with no more than about 10^6 candidate tracks per search window.

B.2.5. The scaling of the number of false tracks with the density of false detections

The final number of false tracks can be computed using eq. B22, after multiplying the normalization constant by p_v^2 to account for velocity filtering. Numerical evaluation shows that the expected number of false tracks per tracklet can be described as

$$N_{\text{tracklet}}^{\text{tracks}} = 2.4 \left(\frac{N_w}{30 \text{ day}} \right)^8 \left(\frac{\rho_{\text{tracklet}}}{450 \text{ deg}^{-2}} \right)^2 \left(\frac{3 \text{ day}}{T_{\text{revisit}}} \right)^2 \left(\frac{1 \text{ deg day}^{-1}}{v_{\max}} \right)^6. \quad (\text{B24})$$

Note the very steep dependence on N_w : the large power-law index (8) is a result of the two powers of 3 under sum in eq. B22, and the scaling of the number of three-night combinations with N_w^2 from eq. B9. The scaling of $N^{\text{falsetracks}} = N_{\text{tracklet}}^{\text{tracks}} N_{\text{tracklet}}$ with the density of false positive detections is very steep, too. Since N_{tracklet} and ρ_{tracklet} are approximately proportional (in the limit $\rho_{\text{ast}} = 0$) to ρ_{FP}^2 (see eq. B5), the number of false candidate tracks approximately scales with ρ_{FP}^6 .

Without approximations, eq. B5 implies a shallower scaling of the number of false candidate tracks, $N^{\text{falsetracks}}$ with ρ_{FP} .

We have determined numerically that the scaling of the number of false candidate tracks per search window with the density of false positives in difference images, as well as other relevant parameters, is well described by

$$N^{\text{falsetracks}} = 4.5 \times 10^6 \left(\frac{N_w}{30 \text{ day}} \right)^8 \left(\frac{\rho_{\text{FP}}}{400 \text{ deg}^{-2}} \right)^{3.7} \left(\frac{\Delta t}{30 \text{ min}} \right)^{2.7} \left(\frac{1 \text{ deg day}^{-1}}{v_{\max}} \right)^{1.3}. \quad (\text{B25})$$

This expression is valid around fiducial values and assumes $\rho_{\text{ast}} = 100 \text{ deg}^{-2}$ and $T_{\text{revisit}} = 3$ days. With fiducial parameters, and when $\rho_{\text{ast}} = 0$, the number of false tracklets per night is $\sim 10^6$, and the number of false tracks per search window with $N_w = 30$ days is about 550,000. For $N_w = 15$ days, the number of false tracks drops to $\sim 2,000$.

Note the shallow dependence on v_{max} – the term v_{max}^6 from eq. B24 is by and large canceled due to dependence of A_S on v_{max} (see eq. B3). We also note that the relevant quantity that determines the number of false candidate tracks is not the ratio of false to real (asteroid) detections in difference images, but rather the overall number (and density) of false detections.

The scaling result given by eq. B25 may prove useful when optimizing cadence and search strategy, as well as for sizing the required computational resources. For example, for the rate of $8,200 \text{ deg}^{-2}$ false positives from Pan-STARRS1, one would expect a factor of 7×10^4 more false candidate tracks than discussed above (that is, about 10^{11}). Even with $N_w=15$ days, the predicted number of false candidate tracks remains of the order 10^9 .

Although MOPS algorithms operate in a different way, these analytic probabilistic considerations explain why the number of candidate tracks produced in MOPS experiments stays approximately the same (to within a factor of two) even when the number of input tracklets per night is increased by about an order of magnitude. With $N_{tracklet}^{tracks} \sim 2$, the number of candidate tracks (both true and false) per search window is about $N^{tracks} \sim 5 \times 10^6$ for $N_w = 30$ days, that is, not overwhelmingly larger than the number of true tracks (500,000). In other words, the ratio of false to true detections of 4:1 generates a ratio of false to true tracklets of 3:1 and a ratio of false to true candidate tracks of 10:1 (for $N_w = 15$ days and $\rho_{ast} = 100 \text{ deg}^{-2}$, the ratio of false to true candidate tracks drops to below 5%).

This similarity in the number of true and false candidate tracks is in good agreement with the results of MOPS simulations³⁴ (though note that those simulations used more aggressive filtering based on “parabolic motion plus topocentric correction” model, and thus obtained a factor of a few lower counts of candidate tracks).

³⁴See the top left panel in Figure 21 in Myers et al. (2013)

REFERENCES

- Annis, J., Soares-Santos, M., Strauss, M. A., et al. 2014, *ApJ*, 794, 120
- Becker, A. 2015, HOTPANTS: High Order Transform of PSF ANd Template Subtraction, Astrophysics Source Code Library, ascl:1504.004
- Becker, A. C., Rest, A., Stubbs, C., et al. 2005, in IAU Symposium, Vol. 225, Gravitational Lensing Impact on Cosmology, ed. Y. Mellier & G. Meylan, 357–362
- Bottke, W. F., Morbidelli, A., Jedicke, R., et al. 2002, *Icarus*, 156, 399
- Connolly, A. J., Angeli, G. Z., Chandrasekharan, S., et al. 2014, in Society of Photo-Optical Instrumentation Engineers (SPIE) Conference Series, Vol. 9150, Modeling, Systems Engineering, and Project Management for Astronomy VI, ed. G. Z. Angeli & P. Dierickx, 14
- Delgado, F., Saha, A., Chandrasekharan, S., et al. 2014, in Society of Photo-Optical Instrumentation Engineers (SPIE) Conference Series, Vol. 9150, Modeling, Systems Engineering, and Project Management for Astronomy VI, ed. G. Z. Angeli & P. Dierickx, 15
- Denneau, L., Jedicke, R., Grav, T., et al. 2013, *PASP*, 125, 357
- Flaugher, B., Diehl, H. T., Honscheid, K., et al. 2015, *AJ*, 150, 150
- Gaia Collaboration, Brown, A. G. A., Vallenari, A., et al. 2016, *A&A*, special Gaia volume
- Goldstein, D. A., D’Andrea, C. B., Fischer, J. A., et al. 2015, *AJ*, 150, 82
- Granvik, M., Virtanen, J., Oszkiewicz, D., & Muinonen, K. 2009, Meteoritics and Planetary Science, 44, 1853
- Grav, T., Jedicke, R., Denneau, L., et al. 2011, *PASP*, 123, 423
- Grav, T., Mainzer, A. K., & Spahr, T. 2016, *AJ*, 151, 172
- Harris, A. W., & D’Abramo, G. 2015, *Icarus*, 257, 302
- Ivezic, Ž., Tabachnik, S., Rafikov, R., et al. 2001, *AJ*, 122, 2749
- Ivezic, Ž., Tyson, J. A., Jurić, M., et al. 2007, in IAU Symposium, Vol. 236, Near Earth Objects, our Celestial Neighbors: Opportunity and Risk, ed. G. B. Valsecchi, D. Vokrouhlický, & A. Milani, 353–362

- Ivezić, Ž., Tyson, J. A., Abel, B., et al. 2008, ArXiv e-prints, arXiv:0805.2366
- Jones, R. L., Yoachim, P., Chandrasekharan, S., et al. 2014, in Society of Photo-Optical Instrumentation Engineers (SPIE) Conference Series, Vol. 9149, Observatory Operations: Strategies, Processes, and Systems V, ed. A. B. Peck, C. R. Benn, & R. L. Seaman, 0
- Jurić, M., Axelrod, T., Becker, A. C., et al. 2016, Large Synoptic Survey Telescope Data Products Definition Document, LSE-163, <https://ls.st/LSE-163>
- Jurić, M., Lupton, R. H., Axelrod, T., et al. 2013, Large Synoptic Survey Telescope Data Management Applications Design, LDM-151, <https://ls.st/LDM-151>
- Jurić, M., Ivezić, Ž., Lupton, R. H., et al. 2002, *AJ*, 124, 1776
- Jurić, M., Kantor, J., Lim, K., et al. 2015, ArXiv e-prints, arXiv:1512.07914
- Kessler, R., Marriner, J., Childress, M., et al. 2015, *AJ*, 150, 172
- Kubica, J., Denneau, L., Grav, T., et al. 2007, *Icarus*, 189, 151
- Miknaitis, G., Pignata, G., Rest, A., et al. 2007, *ApJ*, 666, 674
- Milani, A., Gronchi, G. F., Farnocchia, D., et al. 2008, *Icarus*, 195, 474
- Myers, J., Jones, R. L., & Axelrod, T. 2013, LSST Moving Object Pipeline System Design, LDM-156, <http://ls.st/LDM-156>
- National Research Council. 2010, Defending Planet Earth: Near-Earth-Object Surveys and Hazard Mitigation Strategies (Washington, DC: The National Academies Press), doi:10.17226/12842
- Reiss, D. J., & Lupton, R. H. 2016, Implementation of Image Difference Decorrelation, LSST DM Tech Note, <https://dmtn-021.lsst.io>, doi:10.5281/zenodo.192833
- Schunová-Lilly, E., Jedicke, R., Vereš, P., Denneau, L., & Wainscoat, R. J. 2017, *Icarus*, 284, 114
- Slater, C. T. Jurić, M., Ivezić, Ž., & Jones, R. L. 2016, False Positive Rates in the LSST Image Differencing Pipeline, LSST DM Tech Note, <https://dmtn-006.lsst.io/>, doi:10.5281/zenodo.192828

Stokes, G., Yeomans, D., Bottke, W., et al. 2003, A Study to Determine the Feasibility of Extending the Search for Near Earth Objects to Smaller Limiting Magnitudes., Tech. rep., Report Prepared at the Request of NASA Headquarters Office of Space Science’s Solar System Exploration Division.

Zackay, B., Ofek, E. O., & Gal-Yam, A. 2016, *ApJ*, 830, 27